AIAA AVIATION 2026 Forum, 8-12 Jun 2026, San Diego, Article number 2026-4460
DOI: 10.2514/6.2026-4460

VT Stability Tunnel: Recommendations for CFD Model Validation in Subsonic Wind Tunnels

Adwait Hoge Patil*, Christopher Roy†, William Devenport‡, Aurelien Borgoltz§, and Nanyaporn Intaratep¶
Kevin T. Crofton Department of Aerospace and Ocean Engineering, Virginia Tech, Blacksburg, VA 24060

Davide Di Pasquale‖ and Simon Prince**
Cranfield University, College Road, Cranfield, Bedfordshire, MK43 0AL, U.K.

The current work presents a computational fluid dynamics (CFD) investigation conducted under the NATO Applied Vehicle Technology framework to develop best practices for wind tunnel validation campaigns using the Virginia Tech Stability Wind Tunnel. The study is organized into two components, an empty-tunnel configuration, which forms the primary focus, and a preliminary model-in configuration featuring the Juncture Flow model.

For the empty-tunnel case, a blind validation study was performed to identify and analyze discrepancies between CFD predictions and experimental measurements. Simulations of the as-built tunnel geometry characterize the spatial evolution of static pressure and quantify the influence of wall-induced pressure perturbations within the test section. A complementary investigation examines the flow differences observed under uniform versus non-uniform inflow boundary conditions, providing insight into the sensitivity of test-section pressure behavior to inflow characterization. The paper further consolidates best practices identified throughout the activity, covering meshing, boundary conditions, geometry, post-processing referencing, and experimental comparison.

Preliminary model-in simulations incorporating the Juncture Flow geometry extend the investigation to examine the interaction between model-induced flow features and tunnel wall effects, providing initial validation results and identifying considerations relevant to model-in best practices. Insights from the study will contribute to the development of reliable, reproducible, and traceable best practices for wind tunnel validation campaigns.

*Graduate Student, Aerospace and Ocean Engineering, Virginia Tech, 24060, AIAA Student Member
†Professor, Aerospace and Ocean Engineering, Virginia Tech, 24060, AIAA Associate Fellow
‡Professor and Director of Virginia Tech Stability Wind Tunnel, Aerospace and Ocean Engineering, Virginia Tech, 24060, AIAA Fellow
§Research Associate Professor, Aerospace and Ocean Engineering, Virginia Tech, 24060, AIAA Member
¶Research Faculty, Aerospace and Ocean Engineering, Virginia Tech, 24060, AIAA Member
‖Lecturer in Aerodynamics, Centre for Aeronautics, Propulsion and Power, Cranfield University, UK, Senior AIAA Member
**Professor of Aerodynamics, Centre for Aeronautics, Propulsion and Power, Cranfield University, UK, Senior AIAA Member

Published by AIAA. This is the Author Accepted Manuscript issued with: Creative Commons Attribution License (CC:BY 4.0).
The final published version (version of record) is available online at DOI:10.2514/6.2026-4460. Please refer to any applicable publisher terms of use.

Nomenclature

Variables

C_p	Pressure coefficient	
C_f	Skin-friction coefficient	
I	Turbulence intensity	
k	Turbulent kinetic energy	(m^2/s^2)
M	Mach number	
p	Pressure	(Pa)
r	Grid refinement factor	
T	Temperature	(K)
L	Characteristic length	
u, v, w	Mean velocity components	(m/s)
x, y, z	Cartesian coordinates	(m)

Greek Letters

ρ	Density	(kg/m^3)
τ_w	Wall shear stress	(Pa)

Subscripts

0	Stagnation property
∞	Free-stream property
in, out	Inlet, outlet
ref	Reference property
t	Turbulent
x, y, z	Cartesian components
S	Settling Chamber
C	Contraction

Abbreviations

CRWT	Common Research Wind Tunnel
CFD	Computational Fluid Dynamics
DNS	Direct Numerical Simulation
LES	Large Eddy Simulation
RANS	Reynolds-Averaged Navier-Stokes
RSM	Reynolds Stress Model
VTSWT	Virginia Tech Stability Wind Tunnel
AVT	Applied Vehicle Technology
NATO	North Atlantic Treaty Organization
AOA	Angle of Attack
VVUQ	Verification, Validation, and Uncertainty Quantification
SA	Spalart–Allmaras
VT	Virginia Tech
UI	Uniform Inflow
NUI	Non Uniform Inflow
ET	Empty Tunnel
MI	Model-In
BL	Boundary Layer

I. Introduction

Verification, validation, and uncertainty quantification are essential for establishing the credibility and predictive capability of CFD simulations [1–3]. Verification ensures numerical accuracy and code correctness, validation assesses agreement with experimental observations, and uncertainty quantification characterizes confidence bounds arising from model, numerical, and experimental uncertainties [1, 3]. Foundational studies emphasize that credible CFD cannot rely solely on mesh refinement or code-to-code comparison; systematic comparisons to well-characterized experiments are required to identify model-form errors and quantify total prediction uncertainty [2, 4].

Wind tunnels serve as primary experimental benchmarks for aerodynamic validation due to their controlled, repeatable flow environments and detailed diagnostics. However, facility-induced effects such as wall interference, blockage, and flow non-uniformity features can significantly modify pressure and velocity distributions relative to free-air assumptions [5, 6]. Full-tunnel CFD studies have demonstrated that explicitly modeling the facility is often necessary to isolate such effects and produce reliable CFD to experiment comparisons [5, 6].

Inflow characterization represents a critical contributor to overall facility and modeling uncertainty. Spatial non-uniformities at the inlet plane arising from total-pressure variation, velocity-profile distortions, or unsteady fluctuations can propagate downstream to the test section and substantially influence pressure distribution and integrated aerodynamic forces. Detomaso et al. [7] employed surrogate-based uncertainty quantification techniques in a transonic wind-tunnel environment and demonstrated that even modest inflow inhomogeneities can produce measurable deviations in local pressure fields and drag predictions. Similarly, the NASA Juncture Flow validation campaigns [8, 9] emphasized that precise and repeatable inflow characterization is essential for reducing epistemic uncertainty in wind-tunnel validation efforts.

Inclusion of physically realistic turbulent inflow conditions within numerical simulations is necessary to avoid systematic bias in predicted aerodynamic loads. Rumsey et al.'s [8] Juncture Flow investigations further identify spatial inflow non-uniformity as a dominant source of experimental measurement uncertainty and a key driver of discrepancies between CFD and experimental data.

Geometric fidelity of the facility also affects near-wall pressures. Small deviations like wall bowing, misaligned panels, or test-section contour imperfections can produce localized pressure perturbations and flow separation not captured by nominal CAD geometry [5] [10]. Incorporating as-manufactured (as-built) geometries into CFD models has been shown to reduce CFD to experiment mismatch and enable sound validation outcomes. Accurately predicting pressure perturbations in wind tunnels therefore requires explicit modeling of facility geometry. In this study wall-normal

pressure decay, wall interference, and corner-flow effects rely on analytical or semi-empirical relationships that account for geometric deviations and boundary-layer growth. Including such perturbations in numerical models can reduce observed CFD to experiment discrepancies and improves confidence in validation metrics [5]. Although not all tunnels exhibit these effects, they are pronounced in the VTSWT in part due to the use of pressure probe panels to measure wall pressure. Figure 1 illustrates the surface curvature on the port-side test-section wall and its influence on flow quantities predicted wall shear stress.

Collectively, prior studies highlight three recurring challenges for wind-tunnel validation; facility-induced flow modifications, imperfect inflow specification and variability, and the absence of standardized workflows that integrate facility characterization, experimental uncertainty assessment, and surrogate-enabled uncertainty quantification (UQ) [3, 4, 7–9].

In accordance with these findings, the present investigation incorporates the experimentally measured non-uniform inflow conditions of the VTSWT directly into the boundary conditions for CFD simulations. The facility geometry has been characterized in detail and used to construct high-fidelity computational meshes representative of the as-built configuration [11]. A series of high-fidelity RANS and RSM simulations are conducted using uniform/non-uniform inflow profiles and computational grids are derived from the as-designed and as-built geometry characterization. CFD results are computed for the cases summarized in Table 1. Additionally, an analytical formulation for wall-normal pressure decay is derived for the as-built case that accounts for the pressure perturbations due to facility features.

Table 1 Summary of CFD cases computed.

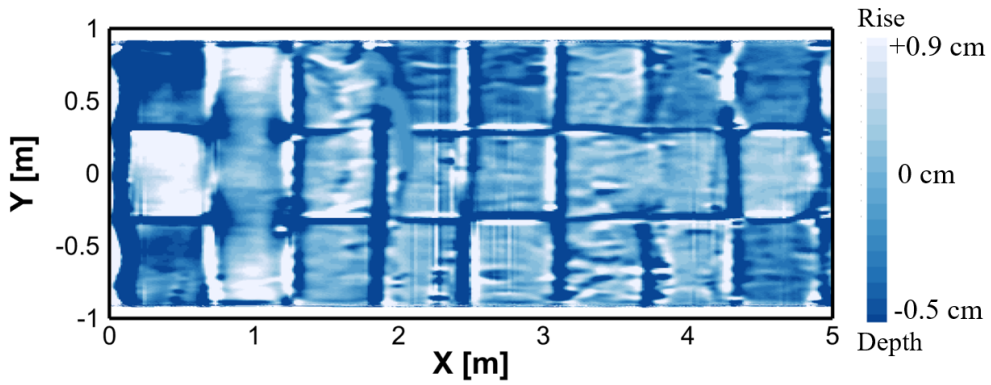
Configuration	Geometry Type	Inflow Type	Reynolds Numbers (Million/meter)
Empty Tunnel	As-Designed	Uniform	1.7, 2.8, 3.9
Empty Tunnel	As-Built	Uniform	1.7, 2.8, 3.9
Empty Tunnel	As-Built	Non-Uniform	1.7, 2.8, 3.9
Model-In at 0^o AOA	As-Designed	Uniform	1.7, 2.8, 3.9

Finally, to assess facility–model interaction effects, additional simulations were performed for a model-in configuration under the same freestream conditions and inflow boundary specifications as the empty-tunnel cases, thereby enabling a direct comparison to isolate the influence of the model and its sting support system on the overall tunnel flow field. At present, the as-designed geometry has been employed for the model-in configuration, while future work will incorporate as-built geometry characterization and non-uniform inflow to more accurately capture the geometric and inflow fidelity observed in the physical facility. The present work forms part of the NATO AVT-387 Research Task Group, with contributions from multiple computational teams performing independent CFD simulations to enable comprehensive uncertainty assessment. All contributing organizations and submission details for the results in the current work can be found in Table 2.

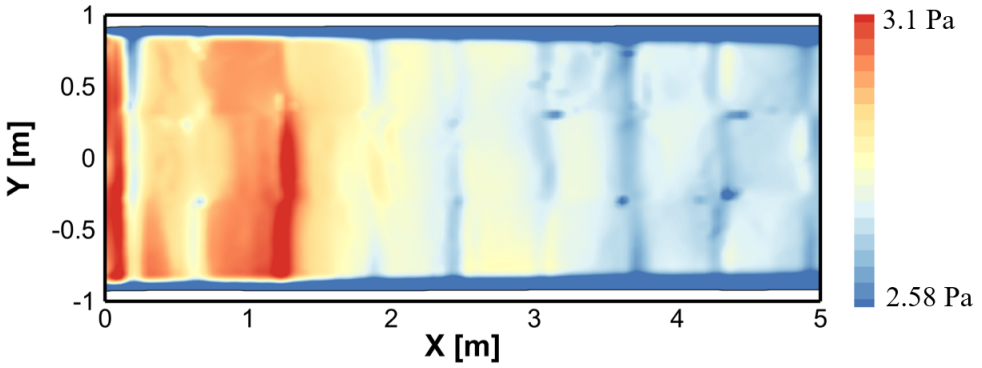
Table 2 Summary of computational contributors for the current VTSWT empty tunnel simulations.

CASE ID	Institution	Name	Model	CFD Code
B	Cranfield University	Tamás Józsa	RSM-KW	Fluent
		Davide Di Pasquale	GEKO-QCR	Fluent
			SST	Fluent
			SA-QCR	Fluent
			SA	Fluent
D	Virginia Tech	Chris Roy	SST	Fluent
		Adwait Hoge Patil	SA	Fluent

The remainder of this paper is organized as follows. Section II describes the Virginia Tech Stability Wind Tunnel facility, the computational setup including the grid family, boundary condition specification, and the measured non-uniform inflow characterization. Section III presents a preliminary overview of the empty-tunnel flow field. Sections IV and V consolidate the best practices identified from the empty-tunnel campaign, covering the synergy between CFD and experiments, reference condition determination, grid construction, turbulence modeling, boundary condition



(a) Surface curvature from LiDAR scan



(b) τ_{wall} from CFD Simulation

Fig. 1 Surface curvature and flow behavior on VTSWT's port side test-section wall

specification, and facility geometry treatment. Section VI presents preliminary model-in results for the Juncture Flow Model installed in the VTSWT, including Reynolds number sensitivity and a direct comparison against the empty-tunnel configuration. Section VIII outlines preliminary best practices specific to the model-in case, with a comprehensive treatment deferred to the full publication.

II. Overview

A. Facility Setup for Virginia Tech Stability Wind Tunnel

VTSWT is a continuous, single return, subsonic wind tunnel located at the Virginia Tech Aerospace and Ocean Engineering Department. It features a 1.83 m × 1.83 m rectangular test section. Flow speeds up to 80 m/s at turbulence levels as low as 0.01% can be achieved, thereby enabling it to conduct tests at Reynolds numbers on the order of 4×10^6 per meter. The facility is equipped with precision wall-pressure instrumentation, a traversing system for flow-field surveys, and interchangeable test-section walls to change between hard wall and anechoic configurations. The tunnel has been extensively used for fundamental aerodynamic studies, model validation, and, more recently, as part of the CRWT initiative to establish standardized datasets for CFD V&V efforts. Figure 2 shows the schematic of VTSWT and the high-speed leg of the tunnel.

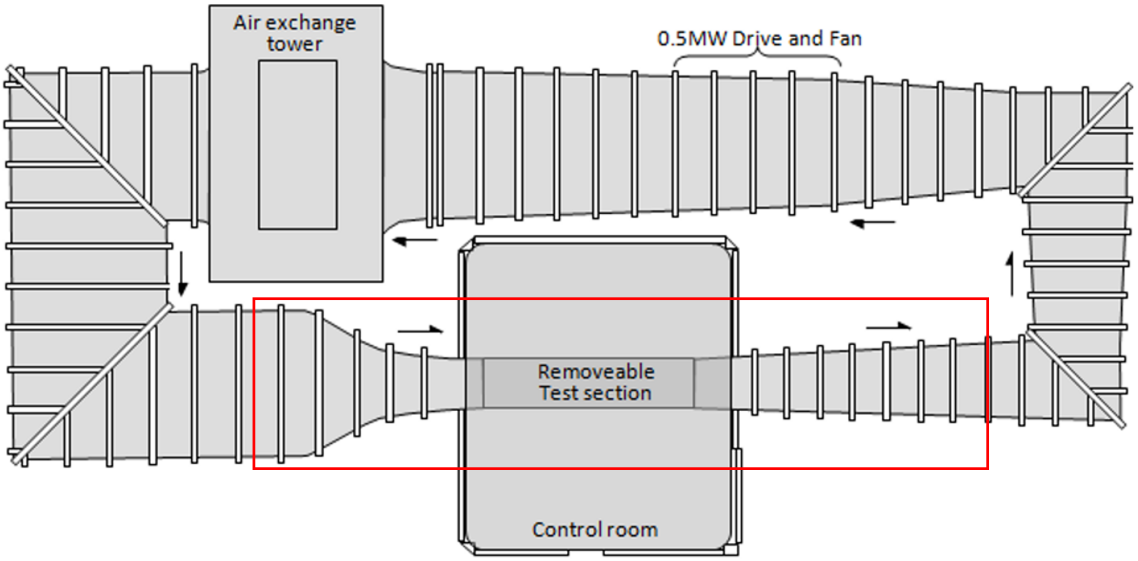
The VTSWT conducted a series of empty-tunnel entries at three Reynolds numbers—1.7, 2.8, and 3.9 million per meter to characterize the empty-tunnel flow behavior and provide a high-fidelity dataset for CFD validation. Boundary conditions were recorded for both uniform and non-uniform inflow cases. CFD comparisons indicate that the

non-uniform inflow data more accurately represents the tunnel operating condition and has therefore been adopted for the UQ analysis.

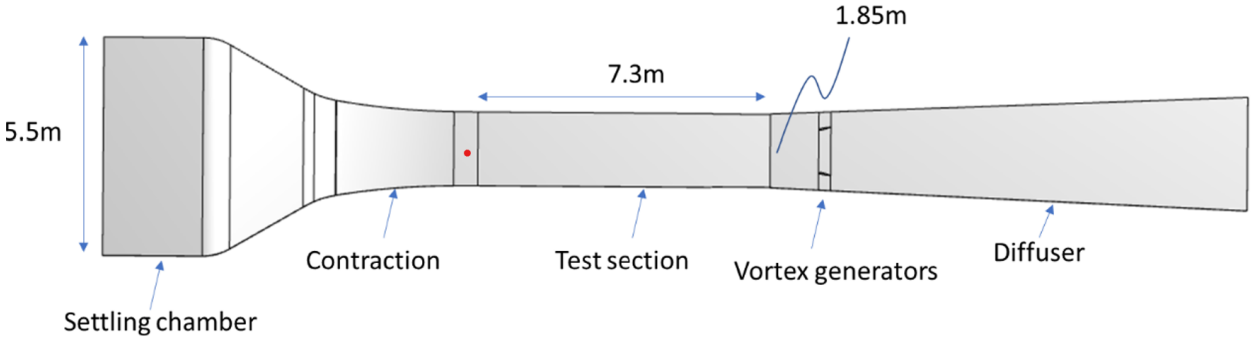
Static pressure measurements were acquired along the centerline of both the port and starboard test-section walls, while corner-flow measurements were obtained at $x = 3.26$ m within the test section. In addition, the boundary-layer profiles were measured at $x = 3.26$ m at the centerline on all tunnel walls (port, starboard, ceiling, floor). These measurements were completed in 2024 as part of the initial baseline characterization effort. Many of these measurements will be repeated for the model-in configuration to enable direct comparisons between the empty-tunnel and model-in cases. CFD extraction and measurement locations for the empty-tunnel case are shown in Figure 3.

In a recent, NATO AVT-391 technical paper, presented at Washington, D.C. , a blind CFD-to-experiment comparison of the empty-tunnel data has been completed and is documented [12]. Two key CFD comparisons were made for the empty-tunnel configuration, first, the as-built versus as-designed geometries to quantify the influence of geometric deviations, and secondly, uniform versus non-uniform inflow conditions to evaluate inflow sensitivity. These results provide the foundation for developing an analytical relationship describing pressure perturbations. The lessons learned from the empty-tunnel blind validation form a significant part of the best practices as detailed in sections IV and V.

For the model-in phase of the validation campaign, the research team is incorporating the NASA JFM [13] [10], a canonical wing–body geometry developed to investigate the complex three-dimensional flow phenomena occurring in the wing–body juncture region, including the onset and evolution of corner separation. The present paper reports only the CFD results for this configuration; no experimental measurements have been acquired for this iteration of the JFM study. The experimental campaign is scheduled for Fall 2026 and will consist of a systematic angle-of-attack sweep from -15° to $+15^\circ$, conducted at the same freestream conditions as the empty-tunnel cases, using the symmetric-wing baseline configuration of the JFM. The primary objectives of the model-in campaign are to acquire high-fidelity surface pressure and velocity data at critical validation locations, and to assess the mutual interaction between the installed model, its sting support system, and the surrounding wind-tunnel flow field. Detailed documentation of the experimental setup, instrumentation, and diagnostics are presented separately in a companion paper at the AIAA Aviation Conference 2026 [11].

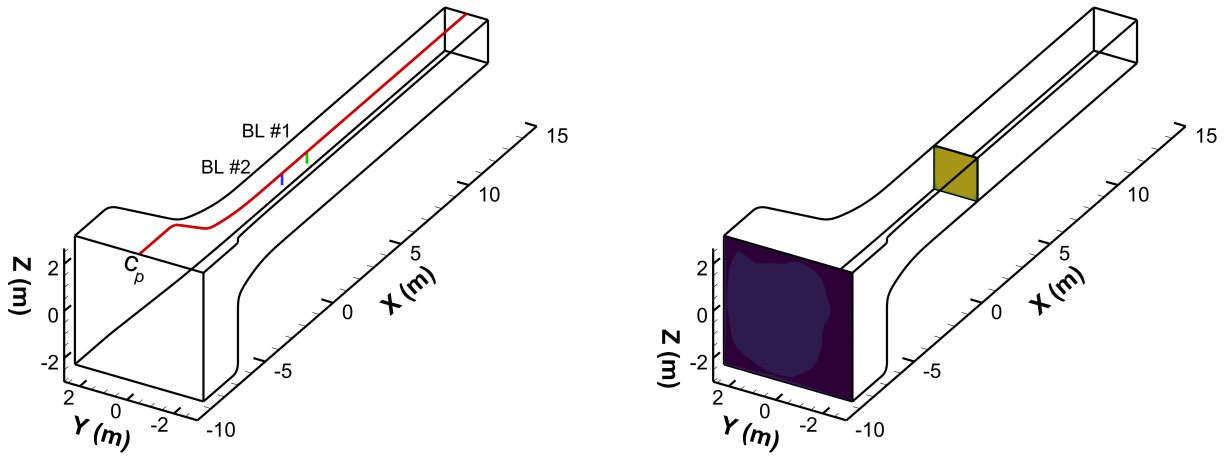


(a) Top-view schematic of the Virginia Tech Stability Wind Tunnel. Red box highlights the high speed leg shown in figure 2b



(b) Nominal geometry of the high-speed leg of VTSWT

Fig. 2 VTSWT schematic and high-speed leg geometry



(a) Extraction locations for C_p and boundary layers on the port side wall. C_p measurements are repeated similarly for the starboard wall, and boundary layer measurements are repeated on all four walls.

(b) Inflow plane and measured contour extraction plane (x = 3.26 m).

Fig. 3 VTSWT CFD data extraction locations.

B. Computational Setup for Virginia Tech Stability Wind Tunnel

1. Computational Grids

A family of eight successively refined meshes is generated to support grid-convergence and uncertainty analysis. Successive grid levels were refined by a factor of $r \approx \sqrt[3]{2}$ in three dimensions (x,y and z). Every fourth grid level is refined by a factor of 2. The mesh family spans from the finest grid (Level 1, ∼640 million cells) to the coarsest grid (Level 10, ∼1.25 million cells). Total nodal count corresponding to the grid levels of the empty-tunnel case can be found in Table 3.

Table 3 Summary of grid levels and corresponding nodal count for empty-tunnel case

Grid Level	Approximate Cell Count (Million)
Level 1 (Finest)	640
Level 2	320
Level 3	160
Level 4	80
Level 5	40
Level 6	20
Level 7	10
Level 10 (Coarsest)	1.25

Systematic mesh refinement was quantified using volume-based metrics following the approach proposed by Eça et al. [14]. Multiple iterations of the grid generation process were performed to ensure near-wall resolution targets were met. For all grids, the first-cell height satisfied $y^+ < 1$, boundary layer clustering resolved the viscous sublayer, and the boundary-layer edge was captured with sufficient wall-normal spacing.

The meshes were developed for both the as-built and as-designed configurations using an identical nodal count. They were employed in a systematic series of RANS simulations. For the quantities of interest in the present study, variations beyond Level 6 were found to be negligible, indicating that the solution had effectively achieved grid insensitivity.

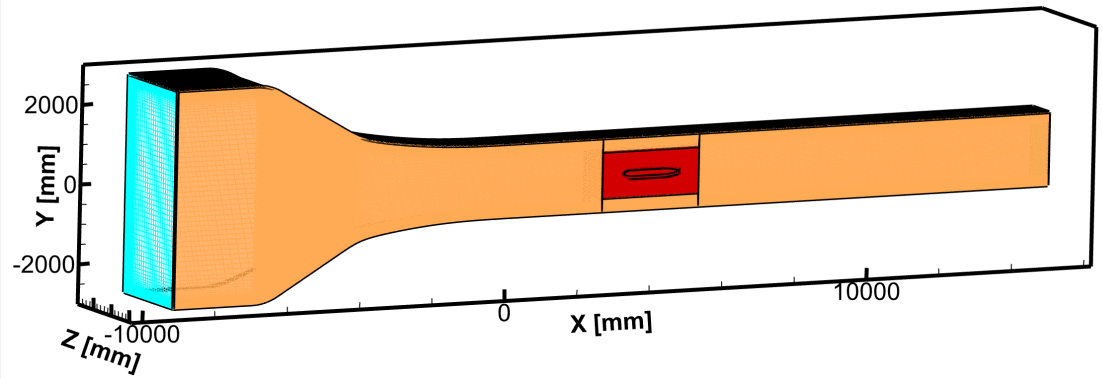
For the model-in configuration, the computational domain was generated by merging the NASA Juncture Flow Model (JFM) grids with the VTSWT empty-tunnel grids. The VTSWT model represents a 2.5% scale of the full JFM geometry, while NASA's configuration corresponds to an 8% scale; consequently, the JFM grids (Figure 4) were appropriately scaled down prior to integration with the tunnel domain.

The JFM grids were refined independently to capture their unique geometric complexity and flow-resolution requirements. These meshes were developed for the as-designed configuration and represent half of the full domain, with a symmetry plane imposed along the tunnel centerline to reduce computational expense. The JFM block employs an unstructured topology with locally refined hexahedral layers near the model surface, generated using Pointwise [15]. The unstructured JFM block was subsequently merged with the structured as-designed tunnel grids, resulting in a seamless hybrid computational domain suitable for high-fidelity RANS analysis.

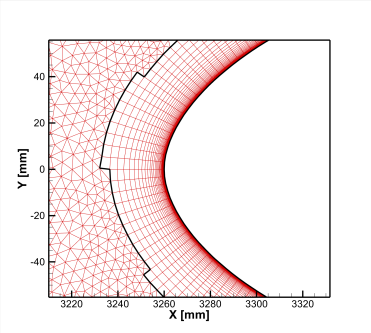
Figure 4, and the total nodal counts for each model-in grid level are summarized in Table 4. The current model-in grids correspond to a 0° AOA configuration, which is maintained throughout the present study. The 0° AOA setup establishes a clean baseline for isolating facility-induced effects such as wall interference and inflow non-uniformity without the added complexity of geometric incidence. A representative view of the computational grid is provided in

Table 4 Summary of grid levels and corresponding nodal count for model-in case

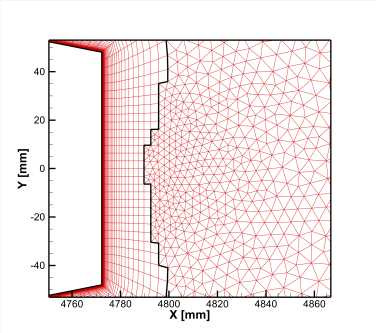
Grid Level	Approximate Cell Count (Million)
Level 3 (Finest)	300
Level 4	120
Level 5 (Coarsest)	50



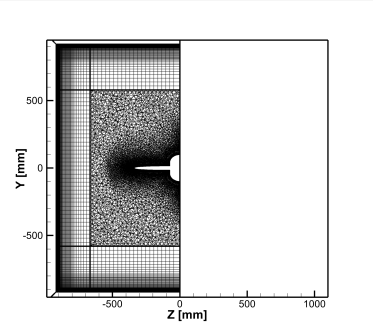
(a) Level 5 VTSWT and JFM model-in grid. The orange-highlighted region denotes the VTSWT tunnel block, and the red region represents the JFM block. Both orange and red regions correspond to symmetry boundary conditions. The blue region indicates the inlet plane.



(b) JFM fuselage leading edge



(c) JFM fuselage trailing edge



(d) JFM+VTSWT grids YZ plane slice

Fig. 4 Model-in test case grids. The top image shows the overall Level 5 grid, while the bottom images highlight detailed fuselage and cross-plane regions.

2. Boundary Conditions

The boundary conditions for the computational simulations were derived from experimentally measured quantities obtained through a series of replicate runs in the VTSWT. The experimentally determined reference quantities are summarized in Table 5. The static pressure listed in the table serves as the reference pressure, used to non-dimensionalize all flow quantities. Other reference conditions such as velocity, density, and temperature were computed from the reference static pressure and measured stagnation conditions using isentropic flow relations.

Table 5 Boundary conditions for the VTSWT empty-tunnel simulations.

	Re = 1.7E6/meter	Re = 2.8E6/meter	Re = 3.9E6/meter
Mach Number* [-]	0.082	0.136	0.193
Stagnation Temperature [K]	297.2	298.4	300.4
Stagnation Pressure [Pa]	94,450	94,359	94,242
Static Pressure* [Pa]	94,009	93,147	91,832

*at X = 3.502 m, Y = -0.608 m, Z = 0 m

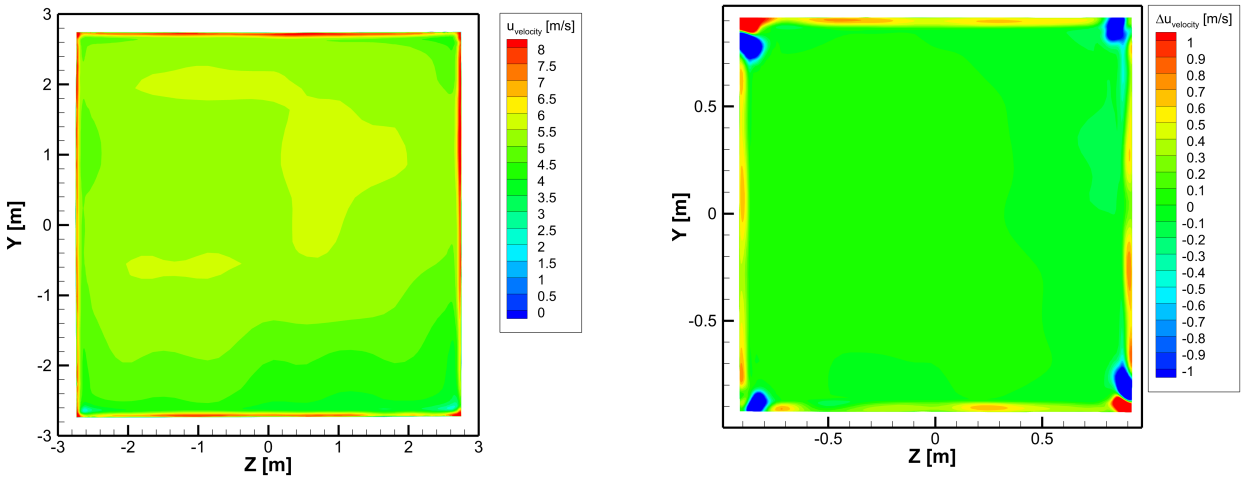
3. Non-Uniform Inflow Specification

To accurately capture facility effects, measurements of non-uniform inflow conditions comprising the static pressure and total pressure were obtained upstream of the tunnel contraction but downstream of the flow-straightening screens.

The measurement plane covered the full 5 m × 5 m tunnel cross-section, from which interpolating functions were developed for each relevant flow property, including axial velocity.

These interpolated fields were used to define the spatially varying inlet boundary conditions for the CFD simulations, representing the as-measured non-uniform inflow configuration. Contours of the inflow velocity magnitude (Figure 5a) reveal localized regions of elevated velocity—often referred to as "jetting"—near the tunnel walls. At the test-section inlet, the difference field $\Delta u = u_{\text{Non-UniformInflow}} - u_{\text{UniformInfow}}$ (Figure 5b) further highlights this near-wall acceleration relative to the uniform inflow case. The "jetting" effect arises because the flow-straightening screens do not extend fully to the wall, leaving a small clearance gap between the frame of the straighteners and the tunnel wall.

The presence of these non-uniformities was found to have a measurable influence on downstream pressure distributions and wall interference effects, further motivating their inclusion in the computational boundary specification. The CFD/boundary condition configurations used in the present work are tabulated in Table 1.



(a) u-velocity contour at the settling chamber inlet plane.

(b) Difference in u-velocity between the NUI and UI inflow profiles at the test-section inlet, $\Delta u = u_{\text{NUI}} - u_{\text{UI}}$.

Fig. 5 Inflow characterization for $Re = 3.9$ Million/meter. (a) Measured non-uniform inflow profile prescribed at the CFD domain inlet. (b) Difference between the non-uniform and uniform inflow profiles at the test-section inlet, illustrating the near-wall acceleration delivered by the non-uniform inflow condition.

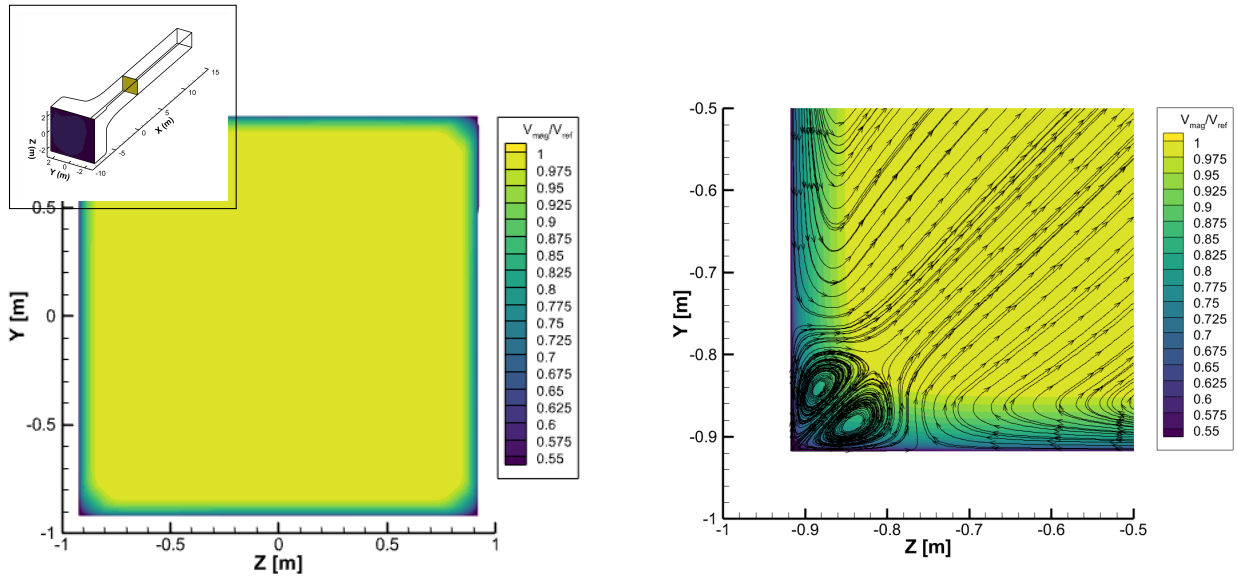
III. Empty Tunnel Results

The empty-tunnel results for configurations mentioned in Table 1 are organized such that supporting evidence for each best practice is presented alongside its corresponding recommendation, with additional supplementary results provided in the appendix. A subset of the results are presented in this section to provide a preliminary overview of the empty-tunnel flow field. Figure 6 presents a contour of the normalized velocity magnitude V_{mag}/V_{ref} on the extraction plane at $x = 3.26$ m, while Figure 7 presents the static pressure coefficient C_p distribution along the port-side wall, spanning the settling chamber, contraction, and test section. Unless otherwise stated, all results correspond to a Reynolds number of Re = 2.8 M/m.

The velocity-magnitude contour indicates that the test-section core is largely uniform, whereas the four corners exhibit pronounced secondary-flow structures, as illustrated by the port-ceiling zoom in Figure 6(b). The corner flow constitutes a critical feature of the facility and is examined in greater detail in subsequent sections, as it accounts for much of the discrepancy between the uniform-inflow and non-uniform-inflow cases.

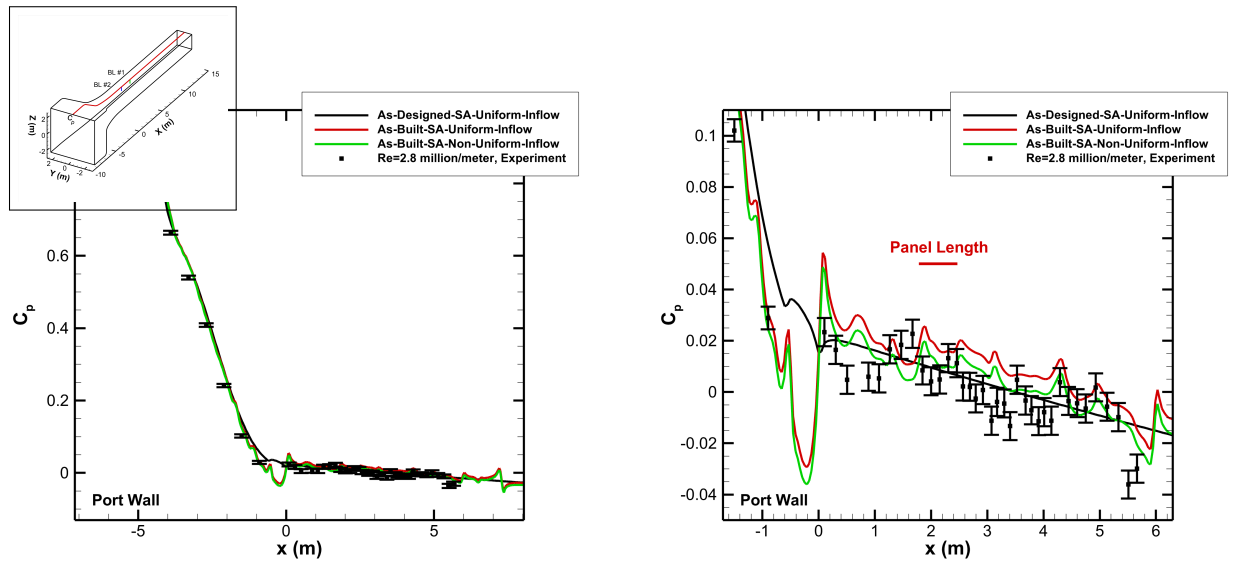
The port-wall C_p distribution exhibits the expected streamwise behavior, as shown in Figure 7. The pressure decreases as the flow accelerates from the settling chamber through the contraction and into the test section, with a corresponding increase in velocity. Results are presented for both the as-designed and as-built geometries, the latter under uniform-inflow and non-uniform-inflow conditions. The as-designed prediction follows a smooth, monotonic decrease, whereas the as-built prediction is markedly more undulatory; this is a direct consequence of the as-built panel

geometry illustrated in Figure 1, where the discrete pressure-measurement panels of the VTSWT introduce localized curvature variations along the wall. The experimental data exhibit a comparable level of waviness, and the as-built CFD prediction reproduces the measurements substantially more faithfully than the as-designed prediction. Agreement is generally within the experimental uncertainty band along the majority of the port wall; the only regions in which the CFD prediction departs from the measurements correspond to the inlet and exit of the test section, where the panel geometry transitions. In particular, near $x \approx 5.5$ m the panel type changes, and over the interval $0 \leq x \leq 1$ m the experimental data indicate a more pronounced acceleration than is predicted by the CFD.



(a) Full plane **(b) Starboard-floor corner zoom.**

Fig. 6 Velocity-magnitude contours at $x = 3.26$ m (UI, SA): (a) the full extraction plane with the extraction-plane location shown inset (top left), and (b) zoomed view of the starboard-ceiling corner.



(a) C_p distribution zoomed to show settling chamber, contraction and test section. **(b) C_p distribution zoomed in at test section.**

Fig. 7 Port-wall C_p distribution at Re $= 2.8$ M/m, with the line-plot extraction locations shown inset on the left panel.

IV. Best Practices for Implementing Computations

A. Synergy between CFD and experiments

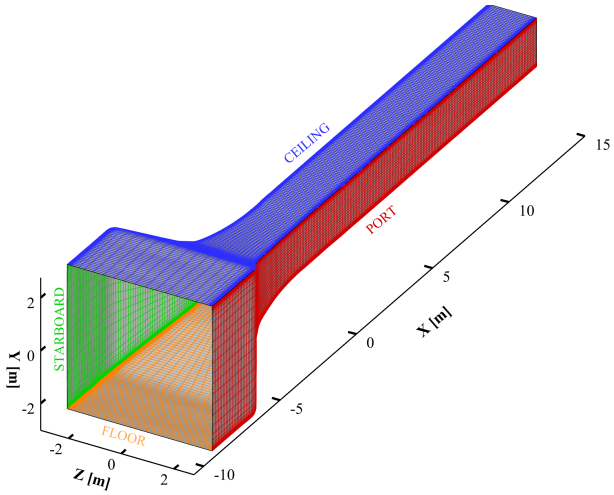
1. *Detailed documentation and clear referencing of coordinate systems should be established early to ensure compatibility between the physical facility and CFD meshes. Computational team's visits to the facility (in-person or virtual) and frequent communication with facility staff can reduce chances of elementary misunderstandings.*

Coordinate system definitions represent one of the most consequential, yet frequently overlooked, points of divergence between experimental and computational workflows. Experimental coordinate systems are typically defined locally, with their origin and axes referenced to convenient features of the test article, instrumentation mount, or facility hardware, and may be redefined between runs within a single campaign as measurement objectives evolve. Computational frameworks, in contrast, demand a single, globally consistent coordinate system that is fixed at the mesh generation stage and propagates through all subsequent solver inputs, boundary condition specifications, and post-processing routines.

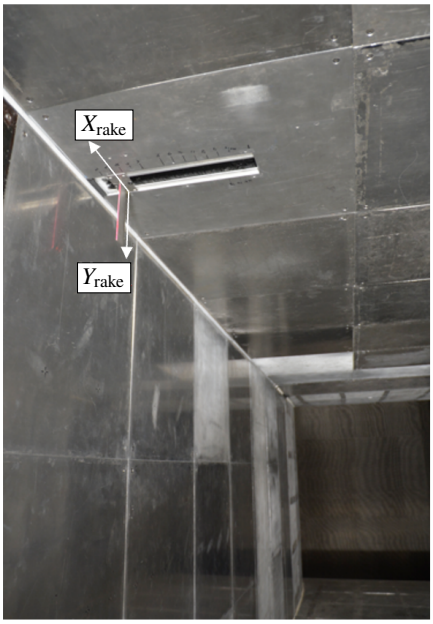
The computational mesh is more rigid of the two, because changing its orientation later requires either rebuilding the mesh or transforming large volumes of output data after the fact. For this reason, the global CFD convention should generally take precedence, and experimental data acquisition should be aligned to it.

Failure to establish this alignment early introduces ambiguities that are notoriously difficult to detect downstream. Discrepancies in axis orientation or sign conventions can produce flow fields and surface distributions that are qualitatively plausible and quantitatively similar in magnitude, particularly on geometrically symmetric or near-symmetric walls, rendering visual comparison between CFD and experimental data an unreliable means of diagnosing the mismatch. The problem is further obscured when a model is included in the CFD domain, as the local pressure response induced by the model can mask coordinate-frame errors in the surrounding wall pressure distribution. By the time such inconsistencies are identified, often only after detailed quantitative comparison fails to converge, substantial computational and experimental resources may already have been expended.

Figure 8 illustrates the global and local coordinate system adopted for the Virginia Tech Stability Wind Tunnel, showing both the CFD mesh frame and the experimental setup to demonstrate the level of documentation appropriate for establishing experimental and computational correspondence. The experimental views additionally highlight the boundary-layer rake instrumentation, which provides highly localized near-wall measurements and therefore requires its own coordinate convention tied to the rake mounting location.



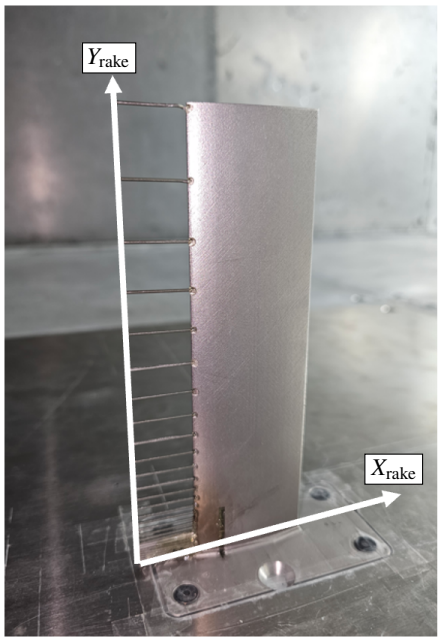
(a) CFD coordinate system.



(b) Ceiling-mounted boundary-layer rake.



(c) Floor-mounted boundary-layer rake.



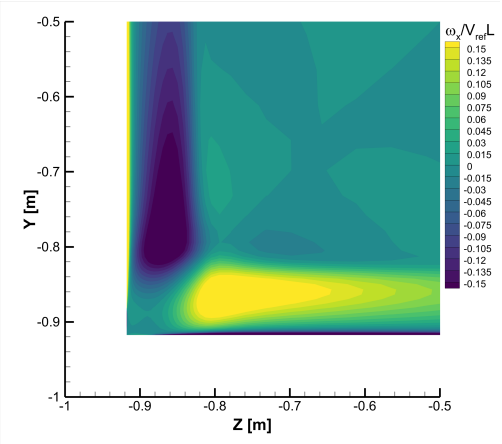
(d) Floor-mounted boundary-layer rake, close-up view.

Fig. 8 Coordinate systems and instrumentation in the Virginia Tech Stability Wind Tunnel. (a) Global CFD mesh coordinate system. (b)–(d) Experimental setup showing the ceiling- and floor-mounted boundary-layer rakes with local rake-coordinate axes X_{rake} and Y_{rake} overlaid; the localized near-wall measurements provided by the rakes require a local coordinate system referenced to the rake mounting location, distinct from the global tunnel frame.

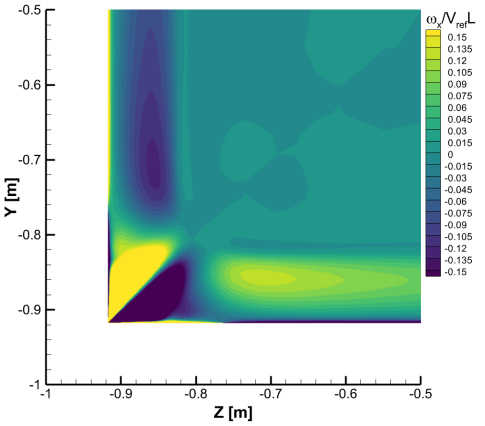
2. *It is extremely important to report and compare all computational and experimental quantities in non-dimensional form.*

No two CFD solutions are produced under identical conditions. Mesh resolution, turbulence closure, and discretization scheme each affect predicted surface loads, separation behavior, and integrated forces, so absolute values reflect the solution procedure as much as the underlying physics.

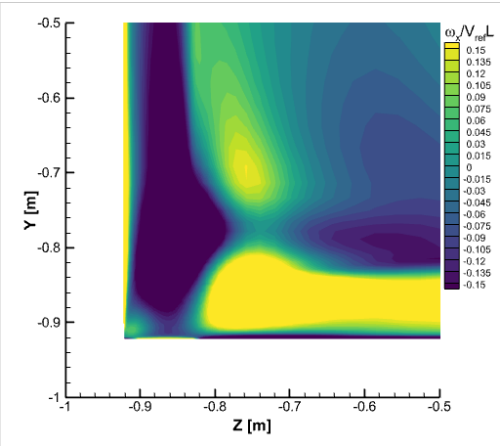
Flow similarity reconciles such disparate results. Flows that match in their governing dimensionless parameters, including Reynolds number, Mach number, and Strouhal number, are physically equivalent regardless of absolute scale or speed. Non-dimensionalization realizes this principle by referring every quantity to a consistent set of reference values, typically the freestream velocity, density, dynamic pressure, and a characteristic length. Community resources such as the NASA Turbulence Modeling Resource [16], the AIAA Drag Prediction and High-Lift Prediction Workshops [17, 18], and the VT–NASA BeVERLI Hill Validation Challenge [19, 20] adopt this convention exclusively, and any study positioning itself against these benchmarks must do the same. The convention should be declared at the outset and applied consistently through every figure, table, and dataset. Figure 9 illustrates this requirement for the present multi-university comparison.



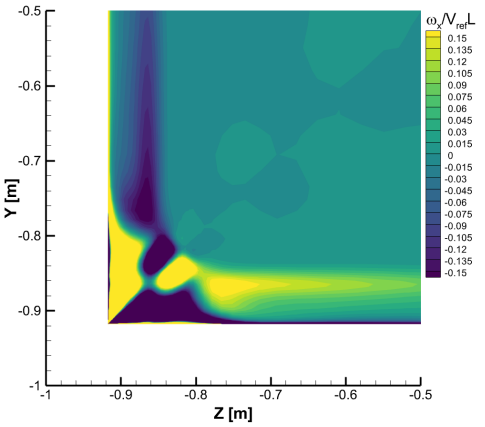
(a) D, As-designed, SA, Uniform Inflow, Empty Tunnel



(b) B, AS-designed, SA-QCR, Uniform Inflow, Empty Tunnel



(c) D, As-built, SA, Non-Uniform Inflow, Empty Tunnel



(d) B, As- designed, RSM, Uniform Inflow, Empty Tunnel

Fig. 9 Streamwise vorticity contour at the port-floor corner, $x = 3.26$ m**,** $Re = 2.8$ M/m**.**

3. Pre-test computations can be valuable to determine which boundary conditions should be measured.

Validation experiments and their computational simulations are most effective when designed in concert. Experimentalists are constrained by available instrumentation and the fidelity with which the flow can be characterized at the inflow, outflow, and bounding surfaces; computational analysts are constrained by the boundary-condition formulations supported by the chosen flow solver and the assumptions embedded within each. Pre-test computations reconcile these competing constraints before measurements are committed to.

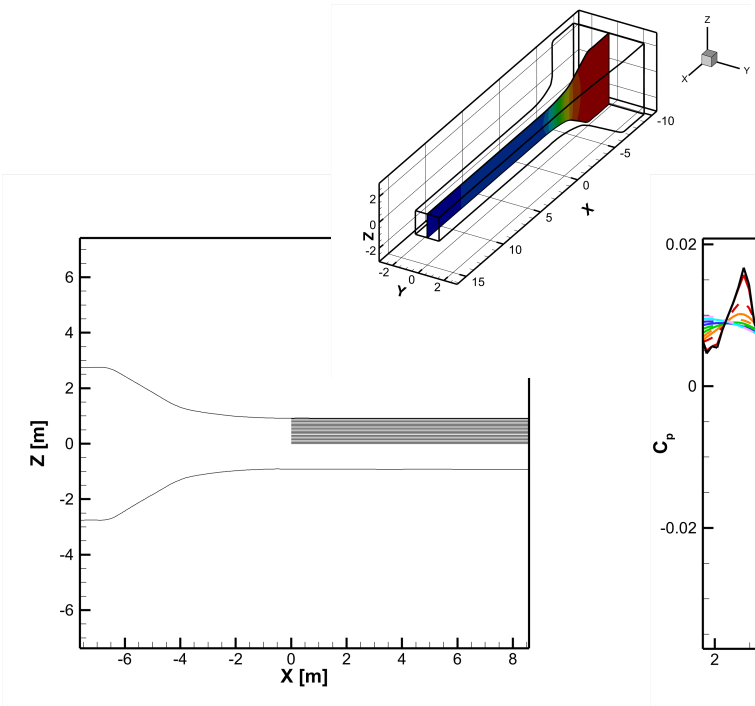
Experimentalists must communicate the spatial coverage, temporal resolution, and uncertainty of each diagnostic, and computational analysts must enumerate the supported boundary-condition options and the physical assumptions underlying each. The simulation boundary conditions should correspond as closely as possible to the experimental conditions, and the measurements should in turn supply the quantities required to specify those boundary conditions directly rather than through assumed values. In the present work, the flow regime permitted the use of isentropic relations and the ideal gas law where conversions between thermodynamic quantities were required.

4. Pre-test computations can be valuable to identify appropriate reference pressure location(s).

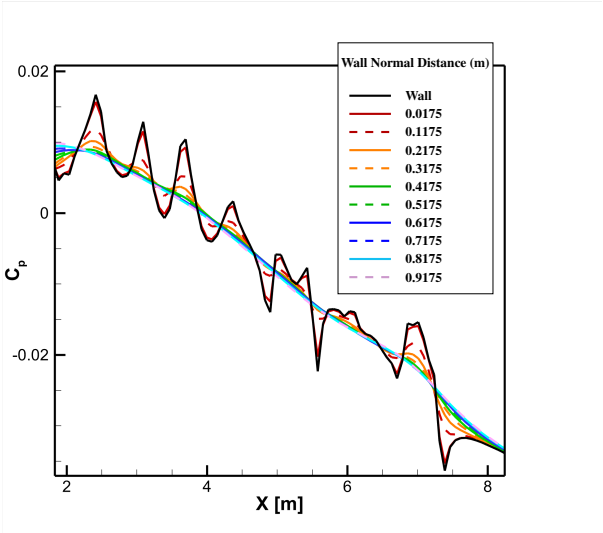
Pre-test CFD of the as-built test section reveals that geometric imperfections in the wall panels introduce localized pressure perturbations that propagate inward and bias any reference pressure measurement taken in their vicinity. The reference pressure in the VTSWT was historically sampled on the test section wall or if measured in the volume, it was approximately 0.305 m [1 ft] from the wall, but the present simulations place this location within the perturbation field of the as-built geometry. The reference was therefore relocated to 0.61 m [2 ft] from the wall, where the perturbation has decayed sufficiently to serve as a freestream reference. Pre-test simulations of this nature can identify the appropriate location *a priori* and eliminate later revisions to test methodology.

Figure 10 summarizes the analysis. Figure 10a shows the extraction strategy, with C_p sampled at 0.1 m [0.328 ft] spanwise increments from the wall to the tunnel midspan. The resulting distributions in Figures 10b and 10d show the perturbation to be largest at the wall and to decay monotonically toward the centerline. The boxed legend entries highlight the curves at 0.3175 m and 0.6175 m from the wall, corresponding approximately to the historical and revised reference stations; the latter exhibits a markedly smaller perturbation.

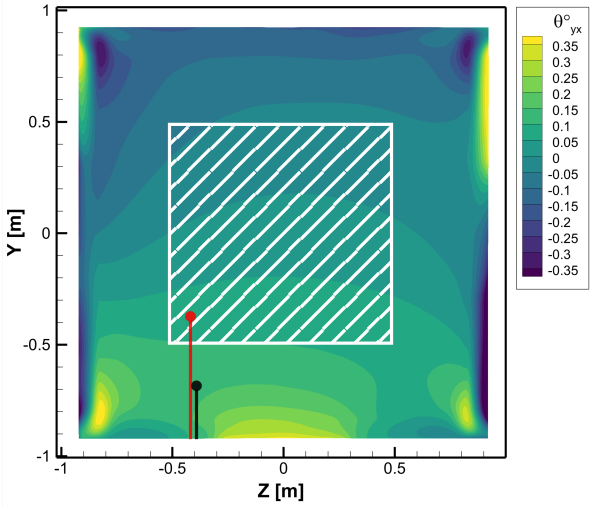
Figure 10c provides complementary evidence from an as-built uniform-inflow simulation. The hatched region indicates the spatial extent over which the perturbation has decayed to acceptable levels. The black arrow marks the historical reference location, lying within the perturbed near-wall region, and the red arrow marks the revised location nearer the core flow. The final selection of a reference location is a facility-specific judgment in which the tolerable residual perturbation is weighed against the practical constraints of the available instrumentation. Pre-test CFD informs that judgment by quantifying the perturbation field.



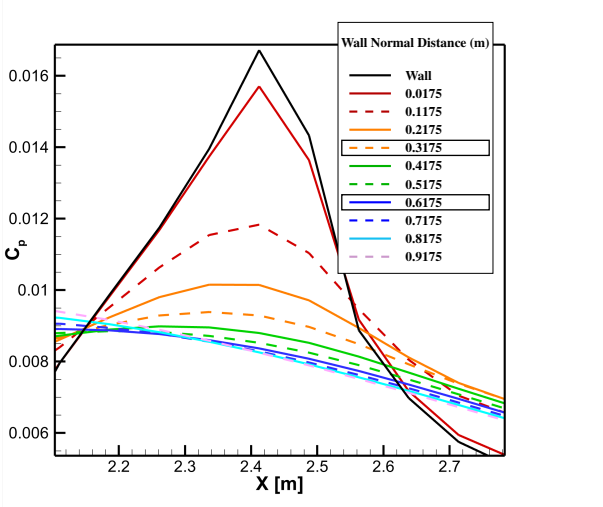
(a) C_p extraction location with slice detail at plane $Y = 0$ (inset).



(b) C_p distribution from port wall centerline to volumetric centerline of the tunnel ($Z = 0.9175$ m).



(c) In-plane flow angularity contour with highlighted region of low pressure perturbation (As-Built, Uniform Inflow).



(d) C_p distribution from port wall centerline to volumetric centerline of the tunnel ($Z = 0.9175$ m), zoomed at fist clear pressure peak in the test section.

Fig. 10 Pressure perturbation analysis for the as-built empty tunnel configuration.

5. Pre-test computations can be valuable to aid in determining sensor location and scaling.

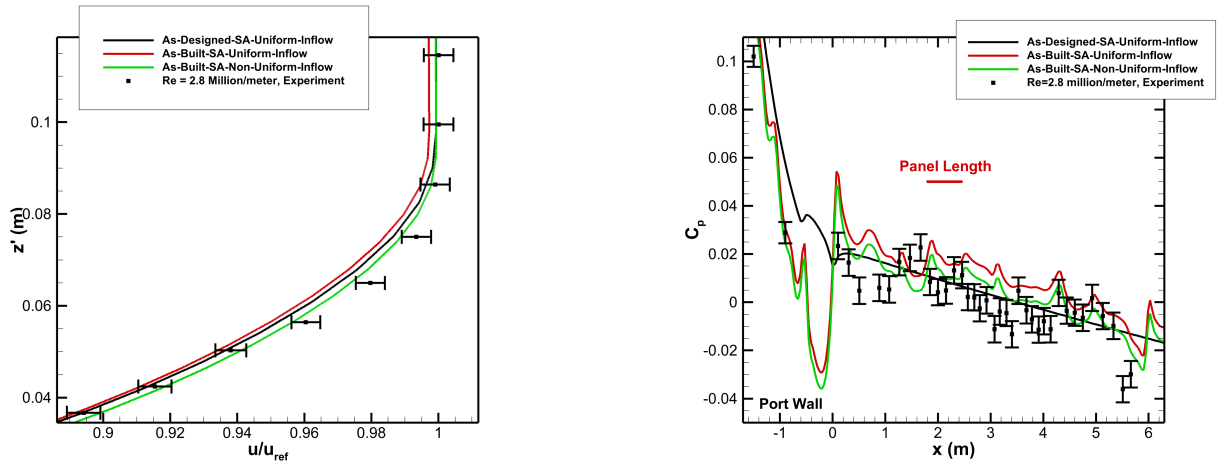
6. Pre-test computations can be valuable to assess assumptions used in post-processing experimental data.

Two assumptions commonly invoked when reducing wind tunnel data are examined here. The influence of as-built wall geometry is confined to a narrow region adjacent to the wall, and that the tunnel inflow can be treated as uniform for the purpose of computing most relevant flow properties. Pre-test CFD provides a means of testing these assumptions directly, before they propagate into post-processed data.

The pressure distributions in Figures 10b and 10d demonstrate that the wall-induced perturbation decays gradually rather than vanishing within a thin near-wall layer. An assumption of negligible wall influence outside a narrow region would therefore admit a non-trivial bias into any measurement taken in the presumed freestream.

The uniform-inflow assumption is examined by comparing simulations with a uniform inlet boundary condition against those prescribing the measured non-uniform inflow. The streamwise velocity contour in Figure 5a shows the measured non-uniform profile, with elevated velocities concentrated near the walls and a comparatively lower-speed core. The corresponding difference field $\Delta u = u_{\mathrm{Non-UniformInflow}} - u_{\mathrm{UniformInflow}}$ in Figure 5b is positive in the near-wall regions, confirming that the non-uniform inflow delivers higher momentum to the wall-bounded portion of the test section than the uniform assumption would imply.

This near-wall acceleration has a measurable downstream consequence. The non-uniform inflow simulations yield wall C_p distributions in closer agreement with experiment than the uniform inflow counterparts (Figure 11a), and the boundary-layer profiles in Figure 11 are measurably thinner under non-uniform inflow on both the port and starboard walls, consistent with the higher near-wall momentum. The two pieces of evidence indicate that uniform-inflow assumptions are not justified by the underlying flow physics in the VTSWT, and post-processing procedures relying on them should be revisited where possible.



(a) BL profile #1 on port wall, zoomed in at BL edge

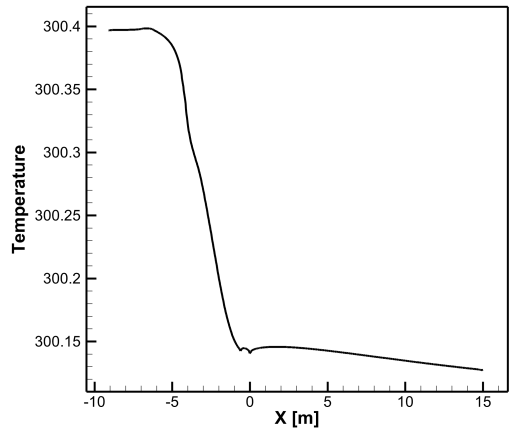
(b) C_p at port wall centerline, zoomed at test-section

Fig. 11 Port-side boundary layer profile and pressure coefficient distribution, zoomed views. z' represents the wall-normal distance for the BL extraction.

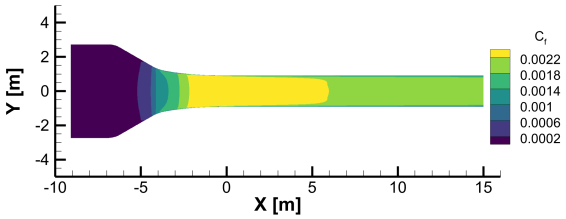
7. Pre-test computations can be valuable to estimate sensitivities of output measurements to flow boundary conditions.

A validation campaign produces a finite set of measurements, and not all contribute equally to discriminating between competing computational approaches. Some quantities vary appreciably across modeling choices such as turbulence closure, geometric fidelity, and inflow specification, and thus serve as useful discriminators. Others are largely insensitive. Pre-test sensitivity studies identify which quantities belong to each category before experimental resources are committed.

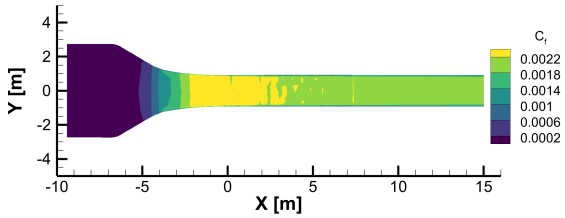
In the present empty-tunnel campaign, temperature distributions were deprioritized on the basis of little variation across the facility (Figure 12a). The skin-friction footprint in Figure 12, which differs visibly between as-designed and as-built geometries under identical closure and inflow, is representative of the sensitivity that motivated retaining wall-pressure and corner-flow measurements as primary validation metrics. Finite experimental resources are best allocated to quantities that actually constrain the validation.



(a) Temperature variation at port wall centerline, Re = 3.9 Million/meter, D, As-Designed, SST, Uniform Inflow, Empty Tunnel.



(b) Re = 3.9 Million/meter, D, As-Designed, SA, Uniform Inflow, Empty Tunnel.



(c) Re = 3.9 Million/meter, D, As-Built, SA, Uniform Inflow, Empty Tunnel.

Fig. 12 Top: Port wall centerline temperature. Bottom: Skin-friction coefficient (C_f) on the port wall.

B. Reference Conditions

1. *Reference condition determination in computations must follow the same procedure used experimentally. Determining reference pressure requires empty test-section tunnel calibration computations to establish calibration between measured and reference pressures, exactly as done experimentally. The process to determine reference pressure will vary depending on turbulence models, tunnel geometry approximations (as-built vs. as-designed), and inflow conditions (uniform vs. nonuniform) and possibly the level of grid refinement.*

In the VTSWT, the freestream reference pressure P_∞ cannot be experimentally sampled directly with a model installed, because the model perturbs the local flow at any candidate measurement location in the test section. The facility therefore ties the freestream condition to two model-independent measurements upstream of the test section, and the same procedure must be reproduced in CFD.

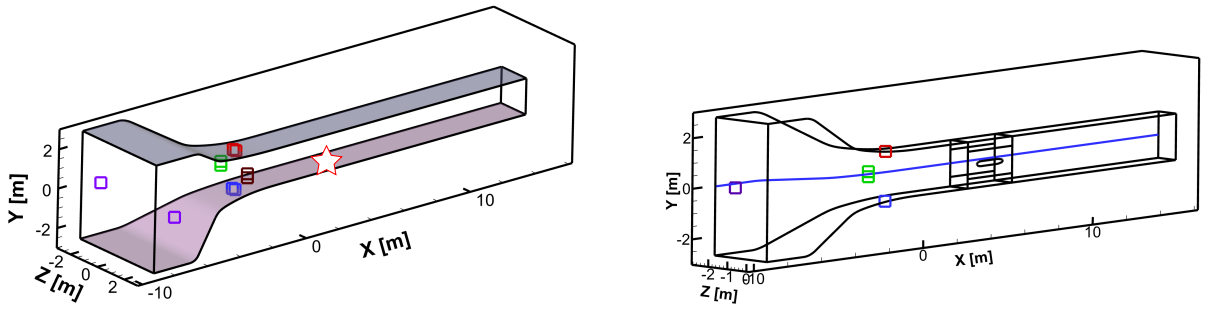
Experimentally the reference velocity is obtained from the readings of the settling chamber and contraction pressures

calibrated against a pitot static probe in the center of the empty test section. The same calibrations process, details of which are provided in [11], is also applied to the CFD.

For the empty-tunnel configuration CFD simulation, P_∞ is sampled directly within the test section, and matching is achieved by adjusting the back pressure until the computed reference pressure matches the experiment at the reference station ($x = 3.502$ m, $y = -0.608$ m, $z = 0$ m). All computed quantities must be nondimensionalized using reference values from the simulation itself, since small errors propagate disproportionately. A 0.1% error in reference absolute pressure produces an 11% error in reference velocity and a 21% error in reference dynamic pressure.

For the model-in CFD case, an empty test-section simulation is first run at the target Reynolds number to record $C_{p,C}^{\mathrm{ET}}$ and $C_{p,S}^{\mathrm{ET}}$. The model-in back pressure is then iteratively adjusted until its upstream coefficients match the empty-tunnel values, ensuring a common freestream condition. Arithmetic details are given in appendix.

The values for the calibration constants, $C_{p,C}^{\mathrm{ET}}$ and $C_{p,S}^{\mathrm{ET}}$, depends on the turbulence model, geometry treatment, and inflow condition, so a separate empty-tunnel calibration is required for each case. The coefficients converge with grid refinement, and the calibration should be drawn from a sufficiently refined level.



(a) Empty test-section configuration showing the contraction ($C_{p,C}$) and settling chamber ($C_{p,S}$) reference stations, together with the freestream reference at the tunnel center of rotation, signified by the red star.

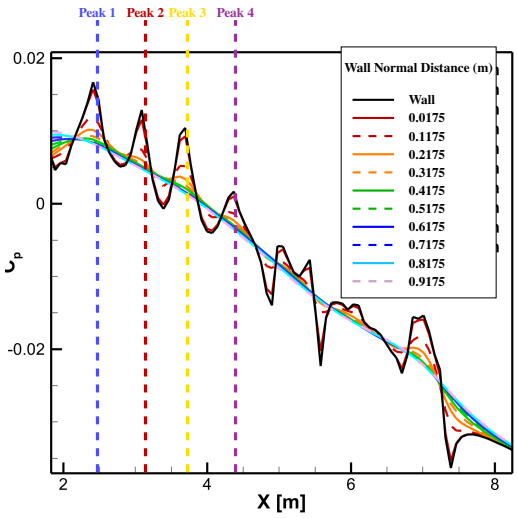
(b) Model-in configuration showing the contraction and settling chamber reference port locations used to compute $C_{p,C}$ and $C_{p,S}$.

Fig. 13 Reference and calibration pressure measurement locations in the VTSWT. The contraction and settling chamber stations provide calibration quantities for both empty test-section and model-in simulations. The red star marks the empty test-section freestream reference station at the tunnel center of rotation.

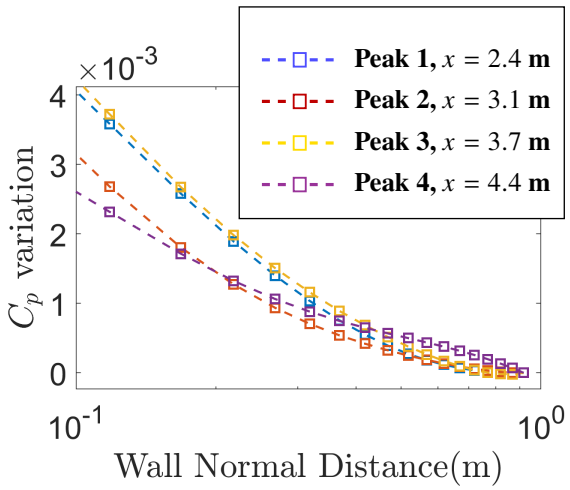
2. *Relying on individual wall static pressures to establish equivalence between computational and experimental conditions can be unreliable since results depend on local imperfections near the sensor. Pressure perturbations from the tunnel wall decay exponentially away from the wall outside of the boundary layer.*

Referencing computational and experimental data through a single wall static tap is unreliable, since the local pressure field is dominated by geometric imperfections in the as-built panels and any equivalence inherits that local sensitivity. Figure 14 provides direct evidence. The spanwise C_p distributions in Figure 14a show the perturbation is largest at the wall and diminishes with wall-normal distance, and the magnified view in Figure 14b shows its amplitude decaying exponentially outside the boundary layer, as expected from potential-flow theory. By a few tenths of a meter from the wall the peak has dropped by nearly an order of magnitude, and at the midspan of the tunnel it is imperceptible.

The upstream contraction and settling chamber stations lie outside this perturbation field, and reference measurements are taken on multiple walls to average out any residual bias. Model-to-experiment equivalence in the VTSWT is therefore established through the upstream calibration rather than through any single wall pressure tap.



(a) Spanwise C_p distributions across the test section, with vertical dashed lines marking the streamwise locations of the four peaks examined in panel (b).



(b) Magnified view of the wall-induced C_p peak across the same spanwise stations in (a), illustrating the exponential decay with distance from the wall.

Fig. 14 Evidence of the wall-induced pressure perturbation and its decay with wall-normal distance. The full spanwise C_p distributions are shown in (a), with vertical dashed lines marking the streamwise locations of the first four clear peaks in the test section. A magnified view of the decay of the peaks at those streamwise stations with wall distance is shown in (b). The peak amplitude decreases exponentially with distance from the wall.

C. Grids: Wall Normal Boundary Layer

1. In constructing computational grids for empty tunnels, key features to resolve include near-wall regions (ensuring wall $y^+ < 1$).

Adequate near-wall resolution is a prerequisite for accurate prediction of boundary layer behavior, wall shear stress, surface pressure, and separation in any wall-bounded turbulent flow. The conventional requirement across the turbulence closures employed here, including Spalart–Allmaras and k–ω SST, is that the first cell-center distance from the wall, in viscous units y^+, lie within the viscous sublayer [16]. A value of $y^+ < 1$ at the first cell, with sufficient cells distributed across the boundary layer, resolves the no-slip condition and the sublayer velocity gradients directly rather than through wall-function relations.

Roy and Blottner [21] identify near-wall y^+ spacing as one of the principal sensitivities that validation studies routinely neglect, alongside discretization error and freestream turbulence specification. Differences between turbulence models reported under insufficient near-wall resolution cannot be unambiguously attributed to the models themselves, since the resulting wall shear stress and downstream flow features may be misinterpreted as modeling deficiencies. Subsonic validation campaigns over airfoils, bluff bodies, and three-dimensional hill geometries consistently report wall-resolved meshes with first-cell $y^+ < 1$ as a prerequisite for meaningful comparison with experimental skin friction and surface pressure data [19, 20]. The empty-tunnel grid adopted here satisfies $y^+ < 1$ along all wetted surfaces, with sufficient cells across the incoming boundary layer to resolve its development.

2. In constructing computational grids for empty tunnels, key features to resolve include the edge of the boundary layer.

Resolving the boundary layer edge is as consequential as resolving the viscous sublayer. While $y^+ < 1$ governs the viscous sublayer resolution, the wall-normal cell distribution across the rest of the boundary layer governs the predicted thickness, the velocity profile in the log and wake regions, and the asymptote to the freestream. This is particularly important in the VTSWT, where the boundary layer evolves continuously from the contraction exit to the diffuser inlet. Table 7 summarizes the wall-normal resolution adopted here, expressed in terms of the local boundary-layer thickness δ.

Values correspond to the coarsest level of the empty-tunnel grid-convergence sequence and represent a lower bound.

Table 6 Recommended boundary layer mesh resolution requirements expressed in terms of $\delta/\Delta y$, where δ is the local boundary layer thickness and Δy is the local grid spacing. Values correspond to the coarsest level of the empty-tunnel grid-convergence sequence and represent minimum recommended resolution.

Table 7 Recommended boundary layer resolution.

Region	Quantity	Recommended Value
Boundary layer edge (wall-normal)	$\delta/\Delta y_{\text{edge}}$	≤ 20
First cell off wall (wall-normal)	y^+	$y^+ \leq 1$
Wall-normal growth ratio	r_y	≤ 1.2
Cells across boundary layer	N_δ	≥ 50

The adequacy of these targets is demonstrated by the boundary-layer comparisons in Roy et al. [12], in which the present grid family predicted empty-tunnel boundary-layer development across a range of test-section Reynolds numbers. Figure 15 shows the wall-normal grid distribution at the coarsest level, with near-wall clustering and cell density maintained out to the boundary-layer edge, and Figure 11a compares the computed profiles on the port and starboard walls against the experimental surveys of Borgoltz et al. [11]. Note that the boundary layer edge value is mentioned for Re = 2.8 Million/meter. In future studies this metric will be generalized and expressed in y^+ terms.

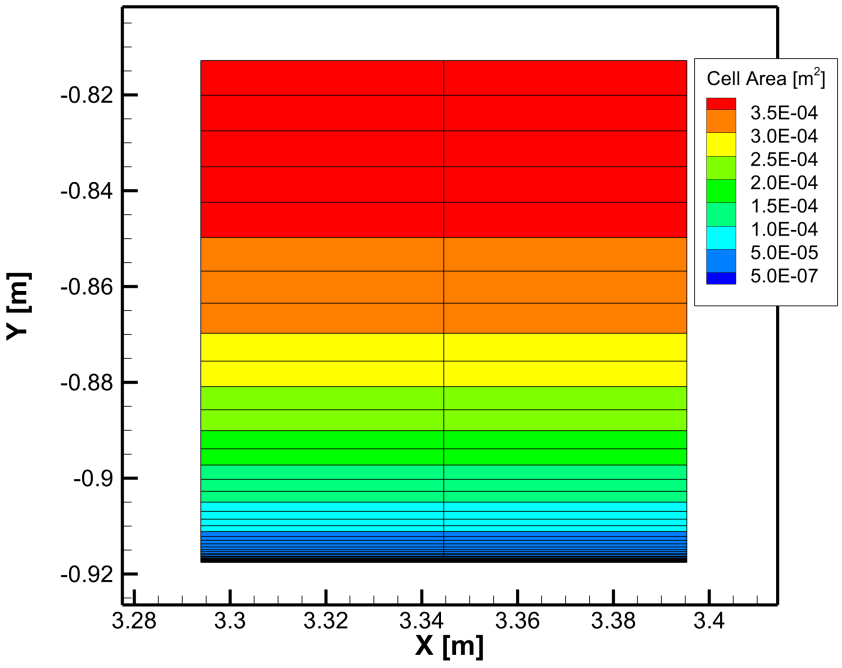


Fig. 15 Wall-normal grid distribution through the test-section boundary layer at the Level 7 of the empty-tunnel grid family, showing near-wall point clustering and cell density maintained through the boundary-layer edge.

D. Grids: High Curvature Regions

1. In constructing computational grids for empty tunnels, key features to resolve include regions of high wall curvature and flow gradients (e.g., contraction and transition to test section).

Grid fidelity in high-curvature regions is bounded by the geometric characterization of the facility. The as-built geometry was acquired through LiDAR surface scans at a nominal axial resolution of 5 mm across the full domain, with a spanwise resolution of 1 mm in the test section and 3 mm in the settling chamber; features below these scales are indistinguishable from measurement noise and are not carried into the CAD reconstruction. Sub-millimeter irregularities such as fastener heads, panel-edge sealant beads, and minor surface discontinuities were further removed during post-processing, since they mesh poorly, produce non-physical pressure perturbations under the present RANS closures, and lie below the resolution at which those closures can produce meaningful predictions. The raw scan and reconstructed surface are shown in Borgoltz et al. [11].

Larger features, in particular the contraction curvature and the contraction-to-test-section transition, were retained and resolved at a coarser scale than the scan. An axial spacing of approximately 50 mm is maintained through the contraction and test section for the coarsest mesh level, sufficient to preserve the upstream flow history conditioning the test-section boundary layer while keeping cell counts tractable, and is visible in Figure 15.

E. Grids: Systematic Refinement

1. A family of systematically refined grids should be used to quantify discretization errors. These should be shown to be small to ensure that conclusions about turbulence models or geometry approximations are not polluted by numerical errors.

Conclusions drawn from a single-grid calculation cannot be separated from the discretization error embedded in that calculation. A turbulence model may appear to outperform a competitor because it does, or because discretization errors are canceling out modeling errors; an as-built geometry treatment may appear to improve agreement because it does, or because the as-built mesh is constructed at a finer effective resolution than the as-designed mesh. Disentangling these contributions requires a systematically refined family of grids on which the discretization error can be estimated and shown to be small relative to the modeling effects under examination.

The present work employs a family of eight grids spanning approximately three orders of magnitude in nodal count, refined at a ratio of $r \approx \sqrt[3]{2}$ between successive levels, with every fourth level corresponding to a refinement factor of 2 in each spatial direction. The refinement is quantified through the volume-based metric of Eça et al. [14]. For every fourth grid level, the largest deviation of the volumetric refinement ratio from the ideal value held to 0.2% ($r_{\text{actual}} = 1.9960$ versus $r_{\text{ideal}} = 2.0000$) and the maximum deviation in representative face areas held to 2.9% ($r_{\text{actual}} = 1.9414$). Wall-normal cell distributions and near-wall clustering were preserved across levels so that the $y^+ < 1$ and boundary-layer edge criteria of the preceding subsection are satisfied throughout. Identical nodal counts were used for the as-built and as-designed grids so that comparisons between the two geometric treatments isolate the geometry effect rather than confound it with resolution.

The multi-team comparison in Roy et al. [12] provides direct evidence that the present grid family is sufficient for the modeling conclusions drawn here. Across nine teams, five flow solvers, and six turbulence closures, the wall pressure coefficient on the finer grids exhibits negligible grid sensitivity, with variations between the finest grids substantially smaller than those attributable to differences between contributors. Boundary-layer profiles at the test-section reference station show similarly weak grid sensitivity, with a small number of grid-sensitive results identified as outliers. For the quantities of interest in the present study, variations beyond Level 6 (~20 million cells) for the empty-tunnel case are below the threshold of practical significance, and Level 6 is therefore adopted as the working resolution. The modeling-effect comparisons reported in subsequent sections, including turbulence closures, as-designed versus as-built geometries, and uniform versus non-uniform inflow, are therefore not contaminated by discretization error.

F. Turbulence Models

1. The use of nonlinear eddy viscosity models (e.g., QCR variants) and Reynolds stress models can resolve secondary flows in test-section corners, unlike linear models. However, the impact of secondary flow may be less important than the inclusion of nonuniform inflow in predicting corner flow.

Standard turbulence models such as Spalart–Allmaras and Menter SST k–ω rely on the linear Boussinesq approximation and cannot predict the secondary flows that develop in the corners of the VTSWT test section. The QCR variants of these models, and Reynolds stress models, relax this assumption and recover at least some of the corner secondary-flow structure.

Figure 16 shows the consequence at the starboard-floor corner under as-designed geometry and uniform inflow, with the experimental measurement in panel (a) as the reference. The standard SA and SST results in panels (b)–(e) show smooth corner boundary layers with no rotational structure, confirmed by the in-plane streamline overlay in panel (f). The RSM, GEKO-QCR, and SA-QCR results in panels (g)–(i) each produce small secondary-flow features near the corner, though none reproduces the pronounced low-momentum bulge visible in the experimental contour.

The gap to experiment is largely closed by replacing the uniform inflow with the measured non-uniform inflow. Figure 17 shows this directly. The top row shows the experimental measurement, the as-designed SA prediction, and its streamline overlay (panels (a)–(c)). The as-built SA simulation under non-uniform inflow in panels (d)–(f) recovers a low-momentum bulge whose location and shape correspond closely to the experimental measurement, and the streamline overlay in panel (e) shows a corner vortex of substantial extent that was absent under uniform inflow. SA-QCR with non-uniform inflow in panels (g)–(h) yields the same outcome, while the as-designed RSM under uniform inflow in panel (i) does not recover the bulge.

Switching from uniform to non-uniform inflow produces a larger improvement in corner-flow agreement than switching from a standard turbulence model to a QCR variant or RSM under uniform inflow. The VTSWT corner flow is therefore driven more by inflow non-uniformity than by secondary-flow physics inside the test section. Practitioners selecting a turbulence model for VTSWT empty-tunnel or model-in simulations should prioritize accurate inflow specification before considering a model upgrade.

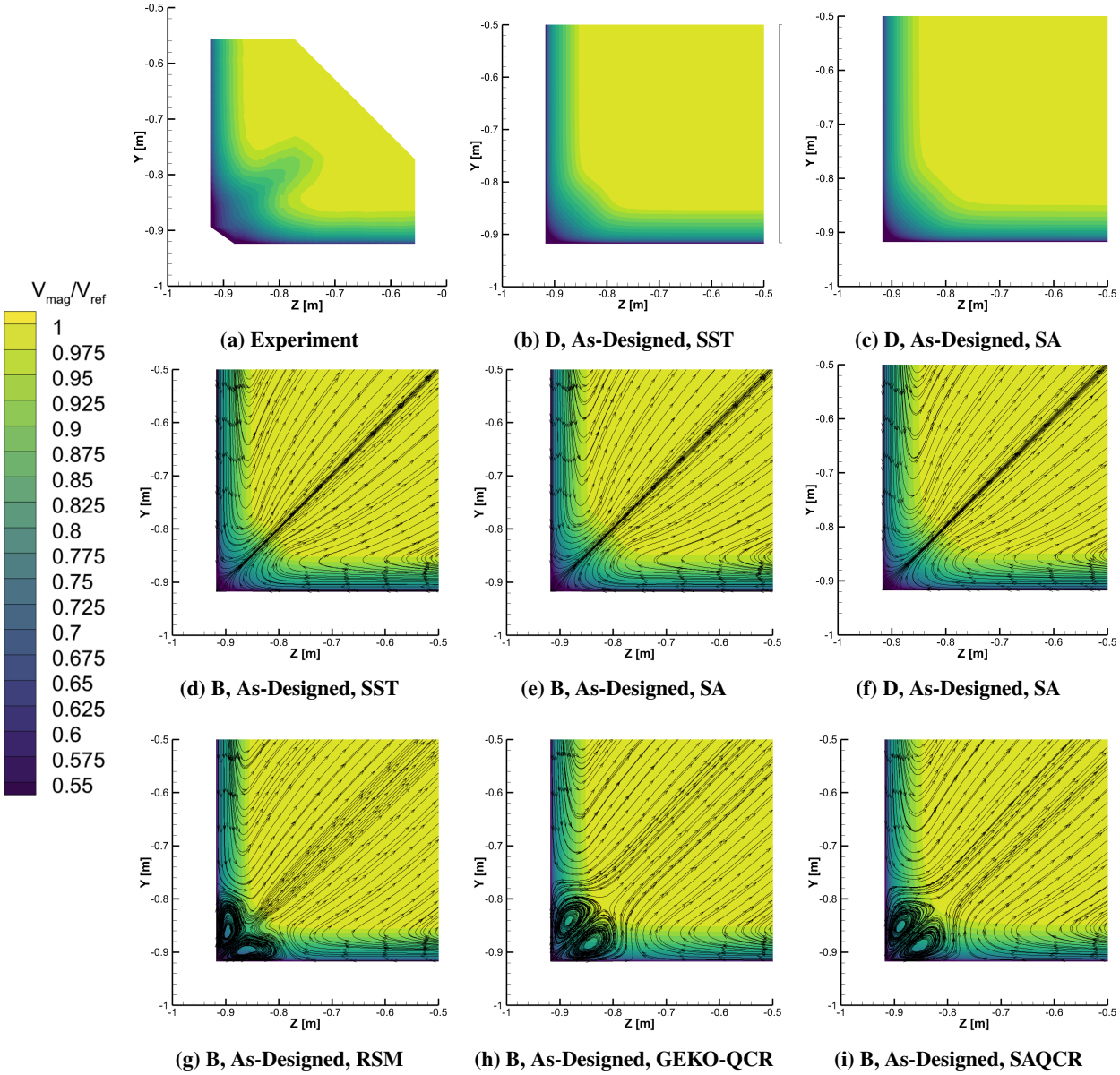


Fig. 16 Contour plots of velocity magnitude at the reference location ($x = 3.26$ m) zoomed in to the starboard-floor corner. Contour plots are shown for $Re = 2.8$ Million/meter, uniform inflow, empty tunnel case.

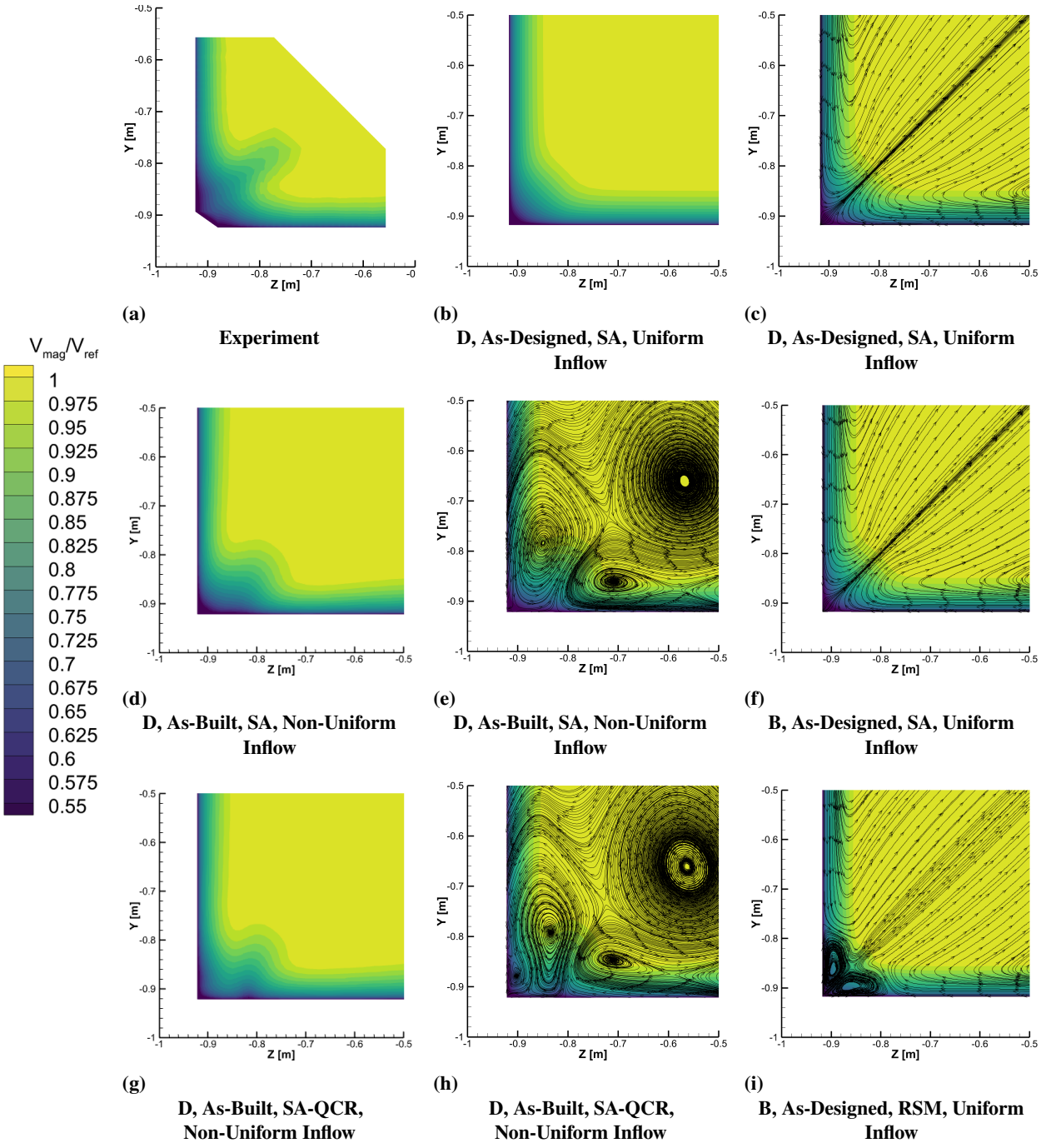


Fig. 17 Contour plots of velocity magnitude at the reference location (x = 3.26 m) zoomed in to the starboard-floor corner. Contour plots are shown for Re = 2.8 Million/meter, empty tunnel case.

V. Best Practices for Computational Modeling of the Facility

A. Boundary Conditions

1. Measurements of the cross-sectional flow (at a minimum, stagnation and static pressure) in the settling chamber can provide important inflow boundary conditions for modeling the high-speed leg.

The choice of measurement plane for inflow characterization involves a trade-off between flow quality, measurement difficulty, and the extent to which the upstream flow history is preserved in the simulation. In the present work, stagnation and static pressure measurements were acquired at the inlet of the settling chamber, upstream of the contraction, and used to construct the non-uniform inflow boundary condition.

The settling chamber was selected over a downstream location for two reasons. First, the flow at the settling chamber inlet is comparatively low-speed, so cross-sectional pressure variations are large enough relative to the absolute pressure level to be resolved with conventional instrumentation; at the test-section inlet, the flow is faster and more uniform, and these variations are correspondingly smaller in absolute terms. Second, the boundary layer at the settling chamber inlet is absent or thin, so the measurement plane is dominated by the cross-sectional non-uniformity the simulation must capture. At the test-section inlet, the boundary layer has already developed through the contraction, and any measurement there mixes the upstream non-uniformity with wall-bounded shear generated inside the simulation domain rather than supplied to it.

The settling chamber measurement comes at a computational cost; the domain must extend upstream through the contraction to the measurement plane, increasing cell count and run time. In the VTSWT, the contraction substantially attenuates the inlet non-uniformity but does not eliminate it, and the residual non-uniformity is sufficient to dominate the corner-flow prediction, as documented in the preceding section. The cost of carrying the contraction in the domain is therefore justified.

A practitioner choosing between settling chamber and test-section inlet characterization should consider the angularity tolerance of the planned measurements. Campaigns involving wall-mounted models or corner-flow measurements should preferentially adopt settling chamber characterization. Campaigns focused on the test-section core, where the inflow effect is comparatively mild, may tolerate the simpler test-section-inlet specification. If test-section wall boundary-layer measurements are to be compared against CFD, settling-chamber characterization is preferable so that the boundary-layer history through the contraction is correctly initialized rather than imposed through an assumed profile at the test-section inlet.

2. Modeling of inflow non-uniformity in the settling chamber appears necessary to replicate details of the test-section corner flows but may not be important for the core flow depending on angularity requirements.

3. The core flow uniformity/non-uniformity in the test section can be more important for sting-mounted models, whereas uniformity/non-uniformity over the entire test section can be more important for wall-mounted models.

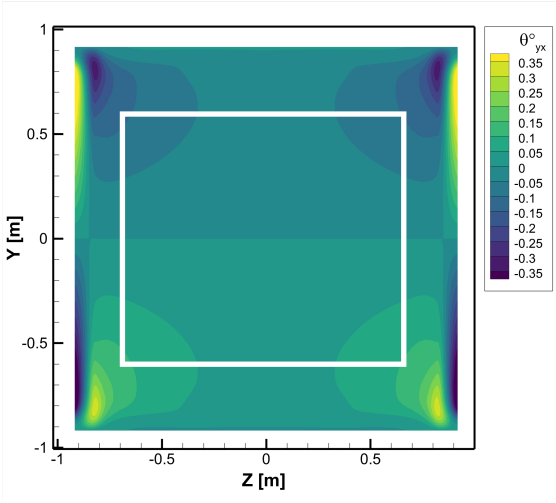
The evidence supporting both best practices is contained in Figure 18, which presents contours of in-plane flow angularity at $x = 3.26$ m for $Re = 2.8 \times 10^6$ m^{-1}. The left column shows the YX-plane angle θ_{YX} and the right column the ZX-plane angle θ_{ZX}. The three rows correspond, in descending order, to as-designed geometry with uniform inflow, as-built geometry with uniform inflow, and as-designed geometry with non-uniform inflow. Contour ranges are tightened to emphasize core-flow variation, and a white square on each panel marks the central region in which the configurations are most easily compared. Within that region, all six panels exhibit angularities below approximately $\pm 0.15^\circ$, with differences between the three configurations at the level of a few hundredths of a degree.

Outside the central square, the angularity changes substantially. Both uniform-inflow rows (panels (a)–(d)) show angularity higher than $\pm 0.30^\circ$ at the corners and approximate four-corner symmetry. The non-uniform inflow row (panels (e)–(f)) departs sharply: angularity is higher than $\pm 0.35^\circ$ in θ_{YX} and $\pm 0.55^\circ$ in θ_{ZX}, the high-angularity regions extend inward along the walls rather than remaining localized at the corners, and the structure is markedly less symmetric, reflecting the asymmetric inflow jetting delivered to the contraction.

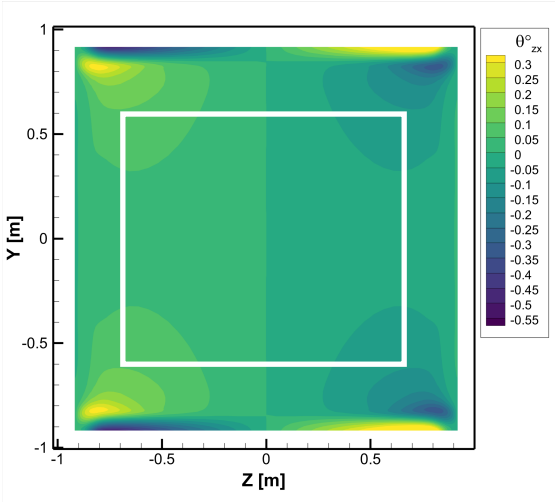
Non-uniform inflow therefore has a small effect on the core-flow angularity, of order a few hundredths of a degree, and a substantially larger effect on the corner-flow angularity. For tolerances typical of empty-tunnel validation, the core-flow difference is below the threshold of practical concern, while the corner-flow change cannot be neglected.

The implications follow directly from the model installation geometry. A sting-mounted model occupies the

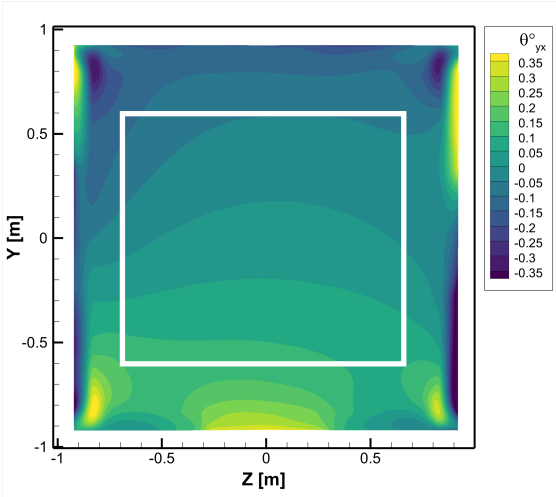
test-section core, so its predicted loads and surface pressures are sensitive primarily to the central-region angularity where the inflow effect is small; uniform inflow simulations may therefore produce acceptable predictions, provided the campaign tolerance is consistent with the few-hundredths-of-a-degree variation in the central square. A wall-mounted model spans from a tunnel wall into the core and is exposed to the full angularity range, including the corner peaks delivered by the non-uniform inflow. The impact of flow non-uniformity is facility dependent and should be assessed for each facility. However, if the flow non-uniformity is a consideration then the selection of an inflow boundary condition for a model-in simulation should begin from the model mounting configuration and work outward to the inflow requirement.



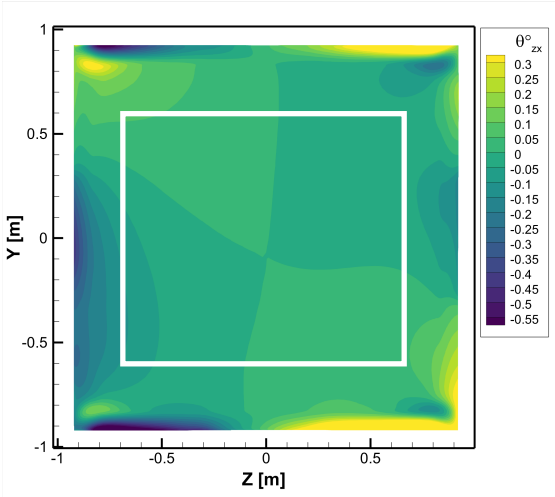
(a) As-Designed Uniform Inflow



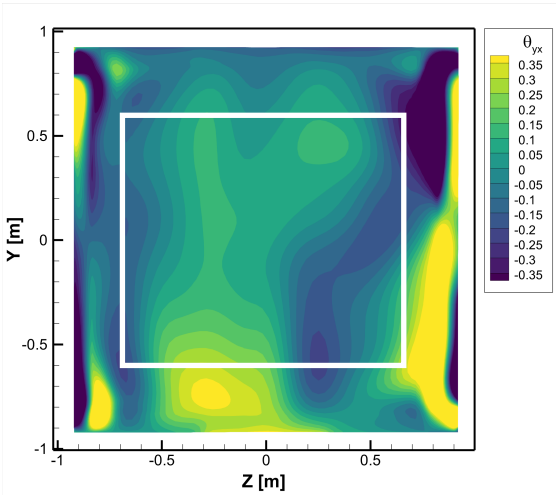
(b) As-Designed Uniform Inflow



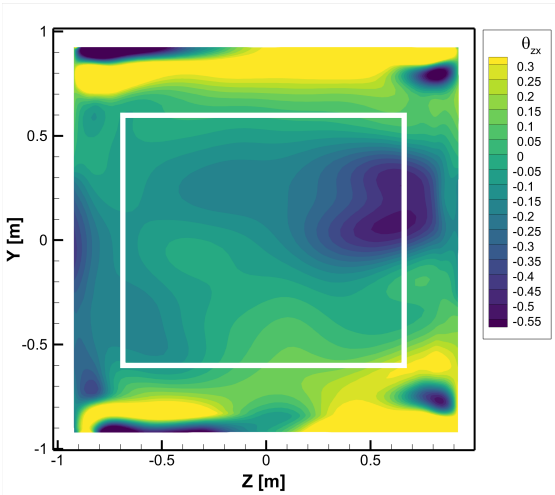
(c) As-Built Uniform Inflow



(d) As-Built Uniform Inflow



(e) As-Designed Non-Uniform Inflow



(f) As-Designed Non-Uniform Inflow

Fig. 18 Contours of flow angularity at the cross-section $X = 3.26$ m for a $Re = 2.8$ Million/meter. The left column shows the YX-plane flow angle (θ_{YX}); the right column shows the ZX-plane flow angle (θ_{ZX}).

4. *Unless analyzing tunnel wall quantities, modeling of inflow non-uniformity appears more important than modeling smaller-scale elements of the as-built tunnel geometry unevenness (e.g., steps between panels and wall bowing). However, the effect of the inflow uniformity and facility geometry on the test section flow may be facility dependent.*

The two principal sources of CFD-to-experiment discrepancy examined in the present work, namely inflow specification and geometric fidelity, do not contribute equally to the overall prediction error. The substitution of measured non-uniform inflow for a uniform inflow assumption produces a larger improvement in predicted flow quality than the substitution of as-built geometry for as-designed geometry under matched inflow conditions.

The wall pressure coefficient comparison in Figure 11b is illustrative. Replacing as-designed geometry with as-built geometry under uniform inflow modifies the predicted streamwise C_p by introducing the panel-induced waviness documented earlier. Replacing uniform inflow with non-uniform inflow under matched as-built geometry shifts the bulk C_p level toward the experimental measurements while preserving the panel-induced waviness.

The boundary-layer profiles in Figure 11a corroborate this finding. The as-built and as-designed predictions under uniform inflow are nearly indistinguishable across the four extraction stations on the port and starboard walls (see appendix), whereas the non-uniform inflow predictions exhibit measurably thinner wall boundary layers consistent with the higher near-wall momentum delivered by the measured inflow profile.

The corner-flow contours in Figure 17 provide the strongest evidence for the ranking. The as-designed and as-built predictions under uniform inflow produce qualitatively similar corner structures, neither of which reproduces the low-momentum bulge present in the experimental measurement. The introduction of non-uniform inflow under either geometric treatment recovers the bulge and the associated secondary structure, bringing the prediction substantially closer to the measurement. The geometric treatment, by contrast, produces no comparable change in the corner flow under matched inflow.

Tunnel wall quantities like the skin-friction contours in Figure 22 show the one quantity for which as-built geometry produces a larger and more visible effect than the geometric treatment elsewhere. The streamwise undulations in C_f on the as-built floor are absent from the as-designed prediction and reflect the panel-induced curvature variations directly. The corresponding non-uniform inflow comparison is not available in the present dataset, and a definitive ranking of inflow versus geometric effects on the wall skin friction therefore cannot be established here. The available evidence on C_p, boundary-layer profiles, and corner-flow velocity is consistent with the inflow effect being the dominant contributor.

This ranking should not be generalized across facilities without examination. The relative importance of inflow non-uniformity and as-built geometry depends on the geometric details of the specific facility, including the contraction ratio, the construction tolerances of the test-section walls, and the design of the flow-conditioning hardware upstream of the contraction. The VTSWT exhibits pronounced wall pressure perturbations from its panel construction and substantial inflow non-uniformity from the clearance gaps in the flow-straightening hardware. In a facility with tighter wall construction tolerances or fully bounded flow straighteners, the relative importance of the two effects may invert. Practitioners are therefore advised to perform pre-test simulations of the type documented in this paper for their specific facility before generalizing the present ranking.

B. Geometry

1. *The likely impact of test-section wall unevenness on the core flow can be assessed using low-order linear methods, which can determine if representation of as-built geometry in computational models is necessary.*

The question of whether as-built wall unevenness produces a core-flow response of consequence to a given measurement can be answered prior to any CFD effort through a potential-flow analysis of the flow over a wavy surface. For a wall whose shape can be represented by a single Fourier mode,

$$\xi = h\, e^{i(k_1 x_1 + k_3 x_3)}, \tag{1}$$

solution of Laplace's equation for the perturbation potential subject to the linearized no-penetration condition, valid in the limit $h \ll L$ with $L \sim 1/k_{13}$ denoting the wall-parallel length scale of the deformations, yields the streamwise velocity perturbation amplitude

$$\left|u_1'(x_2)\right| \;=\; U_\infty\, h\, \frac{k_1^2}{k_{13}}\, e^{-k_{13}\, x_2}, \tag{2}$$

where,

$$\begin{aligned}
\xi &= \text{wall surface displacement,}\\
h &= \text{amplitude of the wall deformation,}\\
k_1 &= \text{streamwise wavenumber of the wall shape,}\\
k_3 &= \text{spanwise wavenumber of the wall shape,}\\
k_{13} &\equiv \sqrt{k_1^2 + k_3^2},\\
x_1 &= \text{streamwise coordinate,}\\
x_2 &= \text{wall-normal coordinate,}\\
x_3 &= \text{spanwise coordinate,}\\
U_\infty &= \text{freestream velocity.}
\end{aligned}$$

The perturbation amplitude in the core decays exponentially with wall-normal distance at a rate set by the wall-shape wavenumber, with the absolute scale fixed by U_∞ and h. The derivation of Eq. (2) from the governing equations can be inferred from the results of Glegg and Devenport [22], Chapter 14.

The analysis was applied to a streamwise section of the VTSWT test section spanning the range over which a sustained sinusoidal wall perturbation could be isolated from the LiDAR-derived as-built surface. The data extraction locations are shown in Fig. 19a, with the corresponding streamwise C_p distributions from the port wall to the tunnel volumetric centerline displayed in Fig. 19b; the dashed markers in Fig. 19b delimit the streamwise window used in the present analysis. Within this window, the wall surface is well represented by a single dominant Fourier mode, as illustrated by the sinusoidal fit overlaid on the wall perturbation in Fig. 19c. Combining FFT spectral analysis with a least-squares sinusoidal fit yielded a dominant streamwise wavenumber $k_1 \approx 9.47\,\mathrm{rad/m}$ and amplitude $h \approx 0.40\,\mathrm{mm}$ at a freestream reference velocity of $U_\infty \approx 46.9\,\mathrm{m/s}$, corresponding to Re = 2.8 Million/meter. The streamwise waviness is taken to dominate over the spanwise component, and k_{13} is taken equal to k_1 accordingly. A vast range of candidate tunnel surfaces can be well decomposed using the above methodology.

The corresponding CFD amplitude was obtained from the difference between the as-built and as-designed solutions at Re = 2.8 Million/meter. The streamwise velocity was extracted along streamwise lines parallel to the port wall at a sequence of wall-normal offsets $x_2 \in \{0, 0.05, 0.10, \ldots, 0.90\}$ m. The wall-induced perturbation was isolated by subtraction,

$$u_1^{\mathrm{pert}}(x_1; x_2) \;=\; u_1^{\mathrm{built}}(x_1; x_2) - u_1^{\mathrm{des}}(x_1; x_2), \tag{3}$$

removing the smooth-wall flow development and retaining only the as-built contribution. The amplitude of u_1^{pert} at each station was obtained by a least-squares fit of the form

$$u_1^{\mathrm{pert}}(x_1) \;\approx\; A\cos(k_1 x_1) + B\sin(k_1 x_1) + C, \tag{4}$$

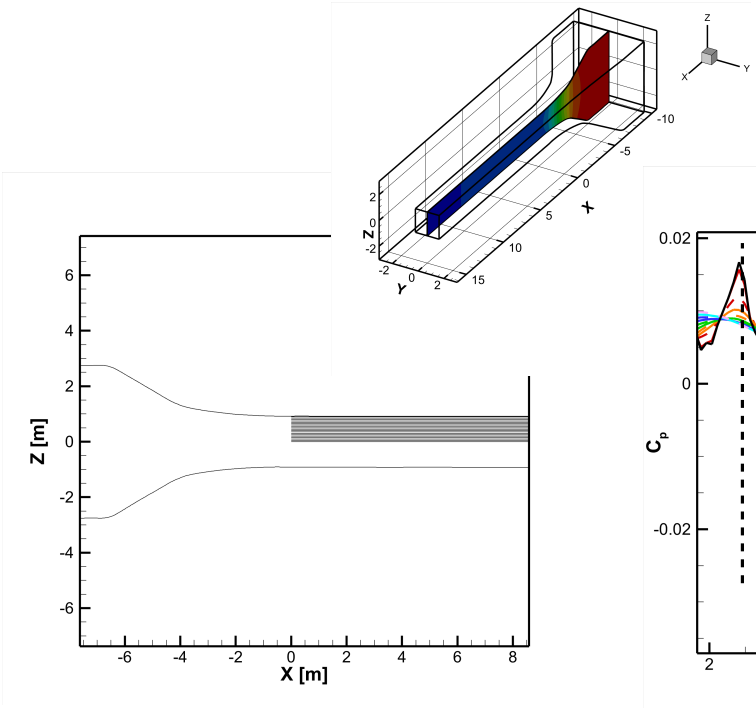
with k_1 fixed at the LiDAR-derived value and the amplitude returned as $\sqrt{A^2 + B^2}$. Fixing k_1 ensures that the CFD and analytical amplitudes are compared at the same spectral mode.

Figure 19d compares the CFD amplitudes with two analytical estimates from Eq. (2) as a function of wall-normal distance, together with annotations marking the boundary-layer edge and the tunnel midspan. The first analytical curve, labeled *Potential flow*, is Eq. (2) evaluated at each wall-normal offset and averaged over the extraction window. The second, labeled *Potential flow "*, is obtained by reconstructing the analytical signal from Eq. (2) and then processing it through the same sinusoidal-fit estimator of Eq. (4) applied to the CFD data, so that both quantities are produced by the same estimator on signals of the same form.

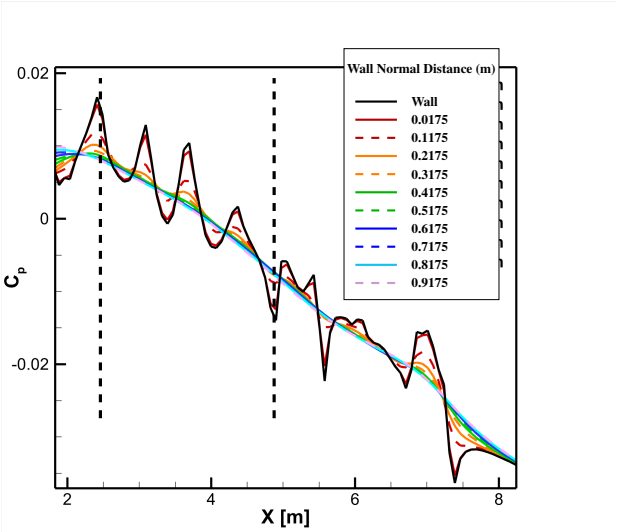
All three distributions exhibit the same exponential decay rate. The sinusoidal-fit estimate falls almost exactly on the CFD result across the full wall-normal range, while the direct evaluation of Eq. (2) consistently overpredicts the CFD amplitude until it drops off by an order of magnitude more than the CFD near the midspan of the tunnel. The offset between the two analytical curves reflects the difference between the peak amplitude given by Eq. (2) and the sinusoidal-fit amplitude of the same signal averaged over a finite streamwise window, rather than a discrepancy between theory and CFD.

The agreement supports two conclusions. First, the linear potential-flow model is quantitatively predictive for the present configuration and can therefore be applied a priori, prior to CFD, to estimate the magnitude of the core-flow

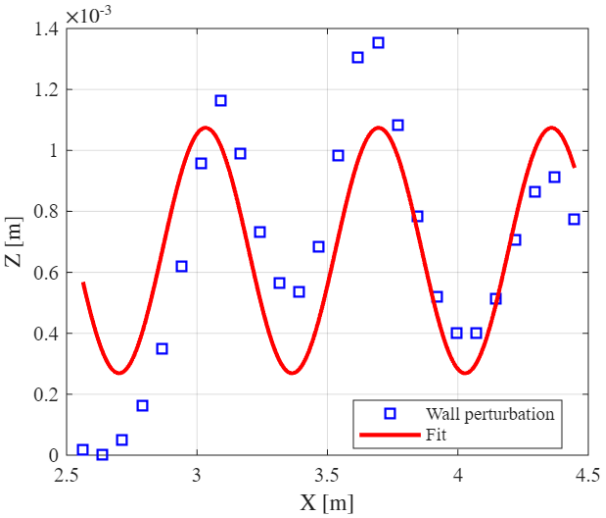
response to a given wall unevenness. Second, the as-built CFD reproduces a physically consistent response to the wall geometry rather than a numerical artifact of the as-built mesh.



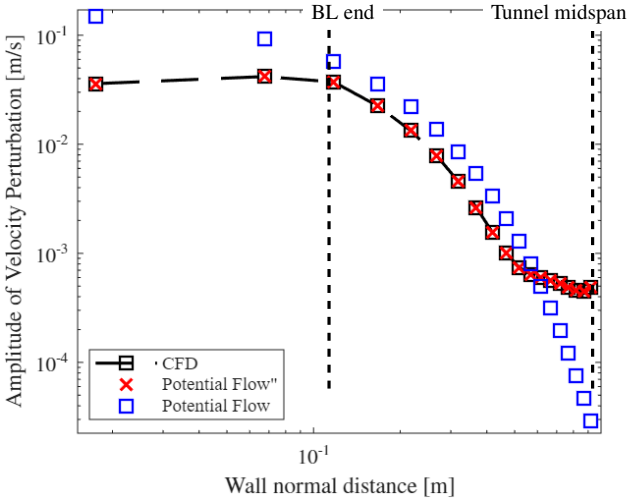
(a) C_p extraction location, with slice detail at plane $Y = 0$ (inset).



(b) C_p distribution from port wall centerline to tunnel volumetric centerline ($Z = 0.9175$ m); dashed lines delimit the streamwise window used for the decay analysis.



(c) Wall perturbation over the selected window and corresponding sinusoidal fit.



(d) Amplitude of the streamwise velocity perturbation as a function of wall-normal distance, with the CFD-derived amplitudes compared against the linear-theory prediction of Eq. (2).

Fig. 19 Potential flow pressure decay analysis for as-built VTSWT walls.

2. *Modeling of the diffuser may be unnecessary if it does not significantly affect the portion of the test-section flow of interest. In the presented empty-tunnel case, extending the test section downstream in an idealized fashion provides an outflow boundary condition where a constant back pressure can be assumed.*

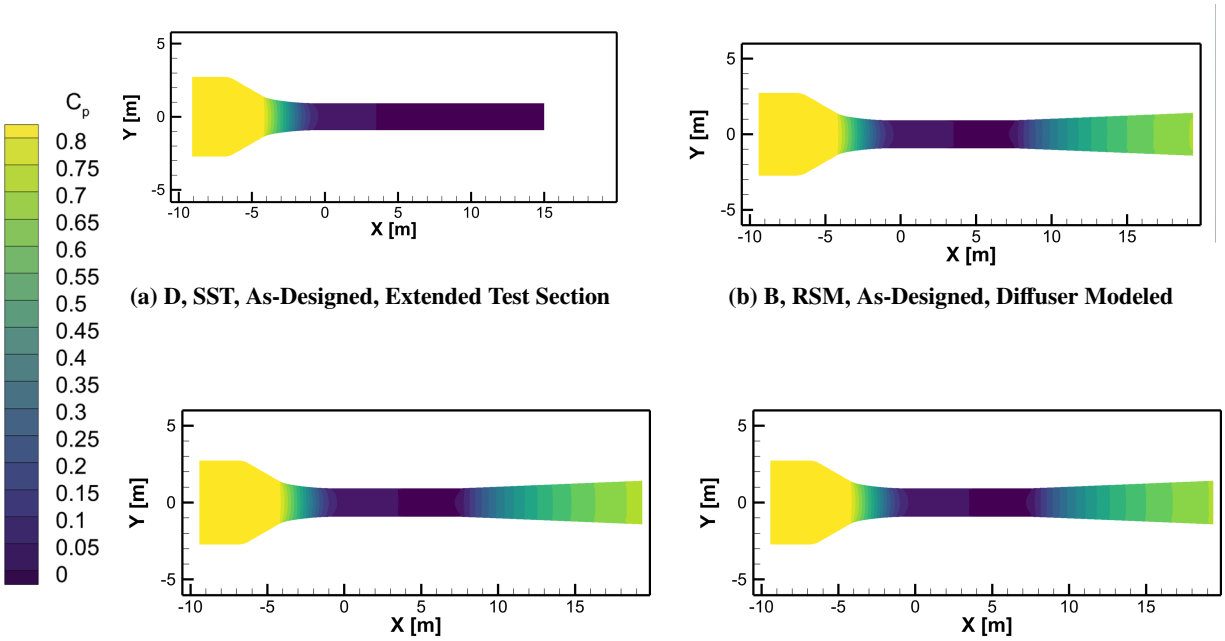
The downstream extent of the computational domain is bounded by the requirement that the outflow boundary condition not contaminate the test-section solution. A constant-back-pressure outflow is the simplest and most robust choice but is physically appropriate only if the outflow plane lies in a region where the flow has recovered to an effectively uniform state. The diffuser, with its area expansion and adverse pressure gradient, is the principal downstream feature that violates this assumption, and its inclusion is a recurring decision in subsonic-tunnel CFD setup.

Two domain-extension strategies were examined. The first retains the diffuser explicitly and applies the outflow condition at the domain exit; the second replaces the diffuser with an idealized streamwise extension of the constant-area test section. The streamwise C_p distributions along the port-side wall are compared in Figure 23. The diffuser-modeled cases (blue curves) exhibit a localized pressure recovery at the diffuser inlet near $x \approx 7.355$ m, while the extended cases (red curves) exhibit a smooth continuation of the test-section pressure decay. The diffuser-modeled cases also show a slight pressure decrease just upstream of the diffuser, attributable to a step in the VTSWT at the end of the test section.

The corresponding centerplane C_p contours in Figure 20, with the zoomed and streamline-overlaid view in Figure 21, cover the as-designed SST computations and the RSM, GEKO and SA-QCR computations that retained the diffuser. The streamlines confirm that, despite the adverse pressure gradient, the flow at the centerplane remains attached throughout the diffuser with no reversal or organized vortical structure. The as-built VTSWT diffuser is equipped with eight vortex generators to maintain attached flow; these were not included in any of the present simulations. The absence of centerplane separation therefore reflects both the benign diffuser pressure gradient at the simulated conditions and the fact that off-centerplane separation tendencies, which the vortex generators are designed to mitigate, are not represented.

Figure 22 compares the C_f along the port wall for the two as-designed configurations. The two distributions agree up to approximately half a test-section width upstream of the physical exit. Downstream of that station, the diffuser-modeled case exhibits a pronounced jump in C_f at the test-section–diffuser junction. The diffuser pressure recovery thus propagates upstream by less than a third-of-the-test-section-width, or about five times the boundary-layer height, beyond which the two strategies converge to within a small offset.

Modeling the diffuser is therefore unnecessary for empty-tunnel campaigns focused on the test-section flow, and the simpler extension approach is recommended on the grounds of reduced cell count and improved mesh quality. For campaigns in which the diffuser flow is itself a quantity of interest, in which a model is mounted near the downstream end of the test section, or in which the pressure recovery propagates further upstream than the third-of-a-test-section-width estimate established here, the explicit-diffuser strategy must be retained. The recommendation applies to subsonic empty-tunnel validation in the VTSWT operating range and should be re-evaluated for facilities with larger diffuser pressure recovery or shorter test-section length-to-width ratios.



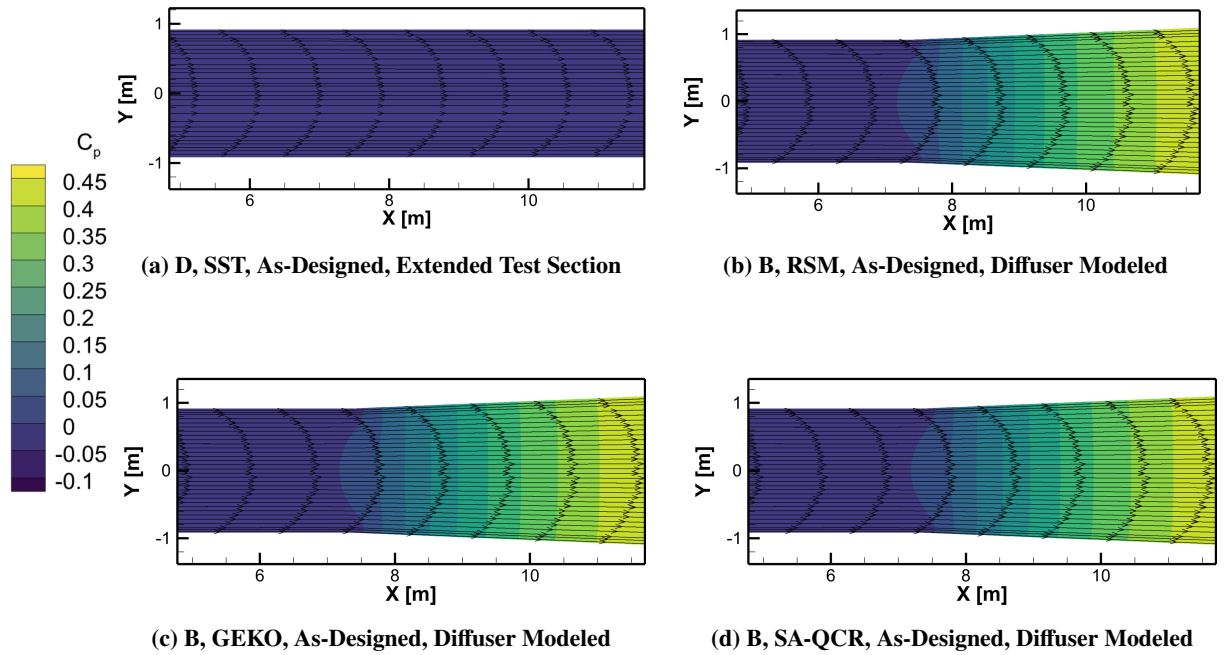
(a) D, SST, As-Designed, Extended Test Section

(b) B, RSM, As-Designed, Diffuser Modeled

(c) B, GEKO, As-Designed, Diffuser Modeled

(d) B, SA-QCR, As-Designed, Diffuser Modeled

Fig. 20 Centerplane C_p contours at $Re = 3.9$ Million/meter. D as-designed extended test section simulation compared with B diffuer modeled simulations.



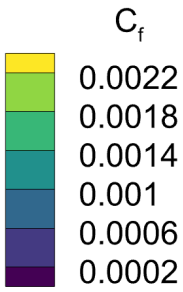
(a) D, SST, As-Designed, Extended Test Section

(b) B, RSM, As-Designed, Diffuser Modeled

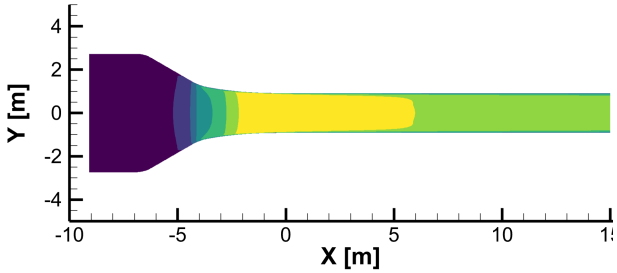
(c) B, GEKO, As-Designed, Diffuser Modeled

(d) B, SA-QCR, As-Designed, Diffuser Modeled

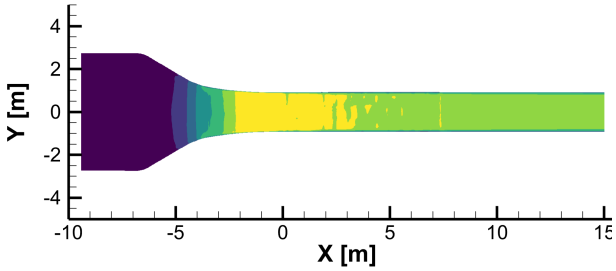
Fig. 21 Zoomed centerplane C_p contours at $Re = 3.9$ Million/meter. D as-designed extended test section simulation compared with B diffuser modeled simulations.



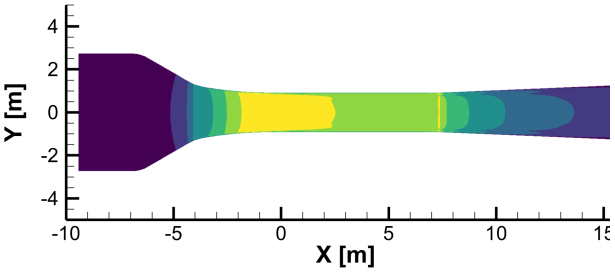
(a) Legend



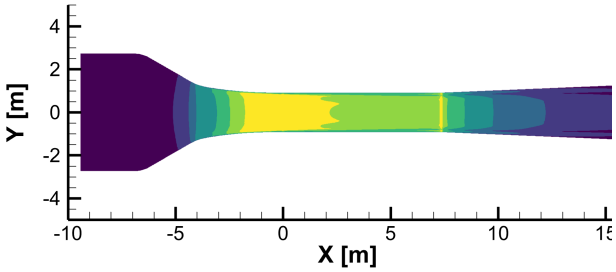
(b) D, SA, As-Designed, Extended Test Section



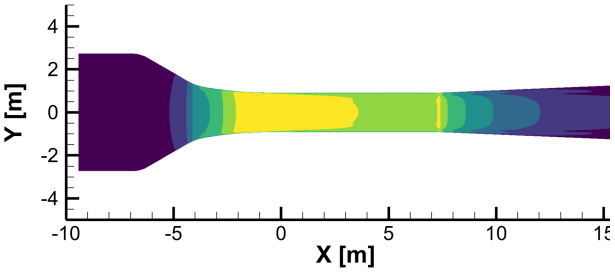
(c) D, SA, As-Built, Extended Test Section



(d) B, GEKO, As-Designed, Diffuser Modeled

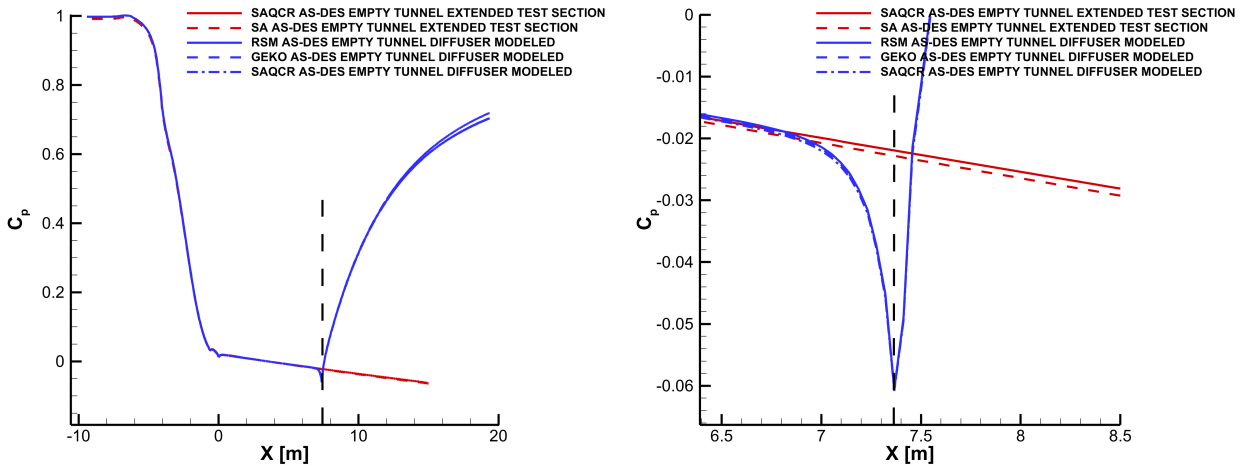


(e) B, As-Designed, RSM, Diffuser Modeled



(f) B, As-Designed, SAQCR, Diffuser Modeled

Fig. 22 Contour plots of skin friction coefficient on the tunnel port wall.



(a) Streamwise C_p distribution along the port side-wall centerline.

(b) Streamwise C_p distribution along the port side-wall centerline. Zoomed in at diffuser inlet ($x \approx 7.355$ m).

Fig. 23 Sensitivity of the port side-wall centerline pressure coefficient, $C_p(x)$, to two geometric modeling choices: (i) explicit inclusion of the downstream diffuser and (ii) axial extension of the constant area test section. Subfigure (b) provides a magnified view in the region of the diffuser inlet to highlight the local pressure recovery induced by the area expansion. Blue line plots show results for modeling choice (i). Red line plots show results for modeling choice (ii).

VI. Model-in Results

For the model-in case, we present preliminary results corresponding to Reynolds numbers of 1.7, 2.8, and 3.9 Million/meter at an AOA of 0°. These simulations were performed at the same freestream pressure as the empty-tunnel cases, enabling direct comparison between the two configurations.

Prior work by Ahmad et al. [23] addressed the effect of wind-tunnel wall boundaries on the simulation of the JFM in the NASA Langley 14 × 22-ft subsonic tunnel at a reference Reynolds number of 2.4 million. Ahmad et at. For in-tunnel versus free-air comparisons, they showed that the computed surface pressure distributions on the wing and fuselage compare favorably with experimental data. The study also found that the inclusion of wind-tunnel walls produced only marginal differences in the size, location, and shape of the separation bubble relative to free-air CFD. Ahmad et al. concluded that the effects of mesh resolution and turbulence modeling outweighed the influence of tunnel boundary conditions on the separation behavior in the juncture region.

Contour extractions are presented for planes upstream of the separation bubble, immediately downstream of the separation bubble, and at the downstream end of the model approaching the sting-support region. These extractions will enable characterization of the approach flow, separation onset, and interaction with the support geometry. Note that the results presented here exclude the sting support geometry. In follow on studies, the configuration will be extended to include the sting support within the tunnel geometry, allowing the interaction between the sting, the model, and the tunnel environment to be resolved and flow features attributable to each element to be isolated. Also, note that the current model-in grids do not resolve the wake behind the model fuselage and hence comparisons for quantities behind the fuselage wake may differ in later iterations of the study.

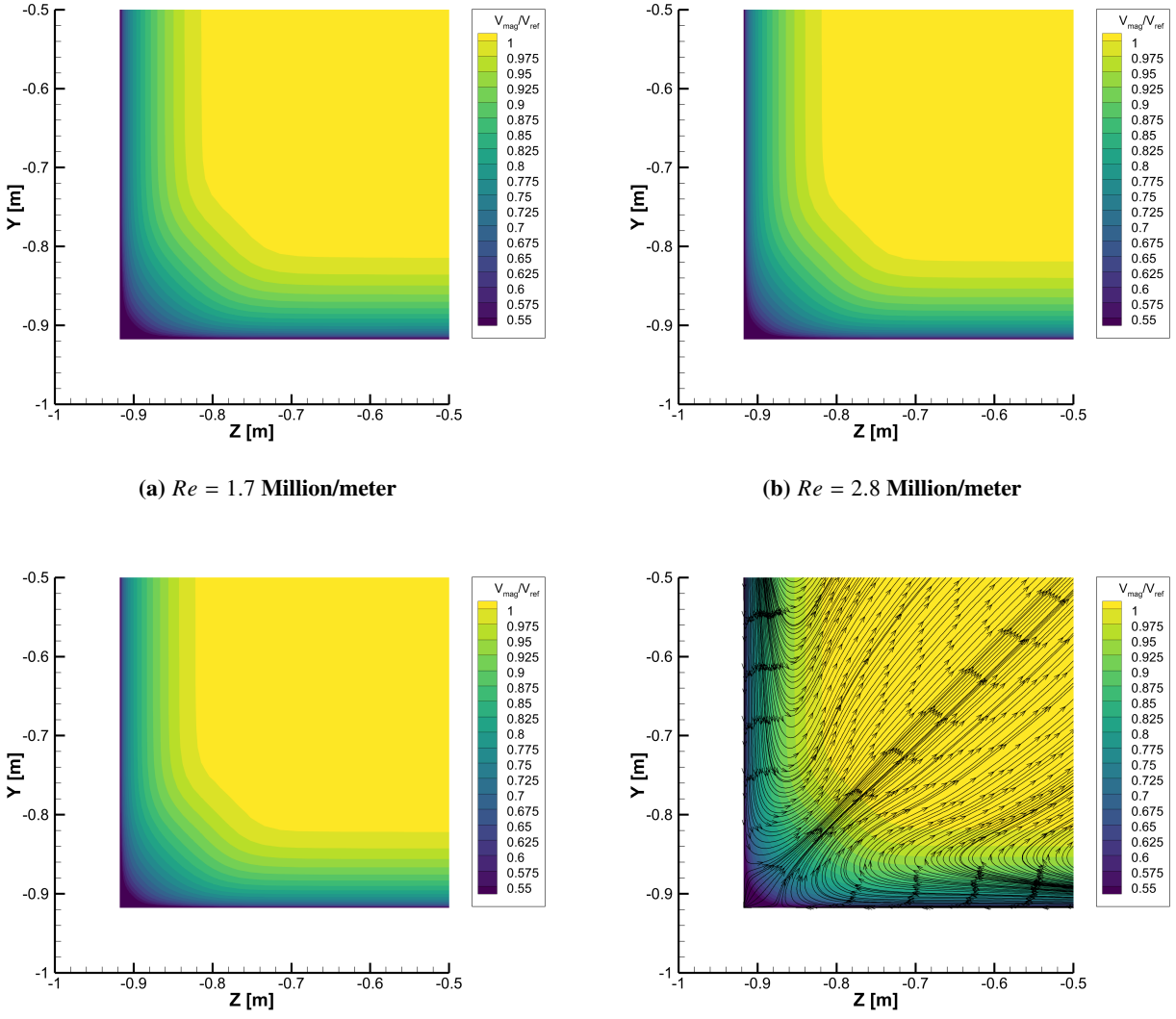
Results from three Reynolds numbers, 1.7, 2.8, and 3.9 Million/meter, are compared to characterize the sensitivity of the model-in flow to operating conditions. Wall pressure distributions, boundary layer profiles, and velocity contours at selected streamwise stations are presented below.

The wall boundary layer thickness decreases with increasing Reynolds number, as expected. The trend is visible in the velocity magnitude contours at $x = 5.0888$ m, Figure 24, and in the corresponding extracted profiles, Figure 26. The differences between cases are most pronounced near the boundary layer edge, while the freestream region collapses to within plotting accuracy when scaled appropriately.

Reynolds number sensitivity is also evident in the juncture region. The pressure disturbance at the wing root grows

in extent with increasing Reynolds number, most clearly at $x = 4.188$ m, downstream of the juncture separation bubble, Figure 25. A qualitatively similar trend is observed at $x = 4.772$ m, downstream of the model, although the fuselage wake is not resolved on the current grids and quantitative interpretation of this station is deferred to subsequent work. Upstream of the separation bubble the contours are nearly indistinguishable across the three cases, indicating that Reynolds number sensitivity in this configuration is concentrated in the separated region and its downstream footprint.

The wall pressure coefficient distributions along the starboard wall, Figure 27, collapse over most of the test section, with a modest elevation at 1.7×10^6 per meter in the region upstream of the model. The wing pressure distributions in Figure 28a -28d, show a decrease in C_p at the leading edge with increasing Reynolds number, consistent with the increase in local flow speed. These observations are consistent with the trends reported in the NASA Juncture Flow computational and experimental campaigns [13].



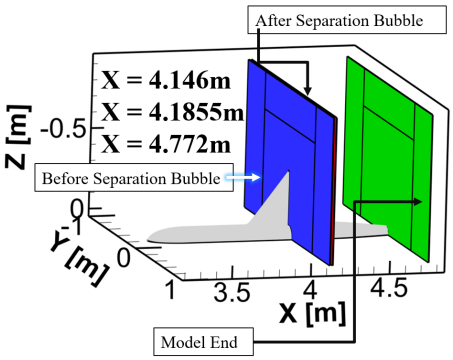
(a) $Re = 1.7$ **Million/meter**

(b) $Re = 2.8$ **Million/meter**

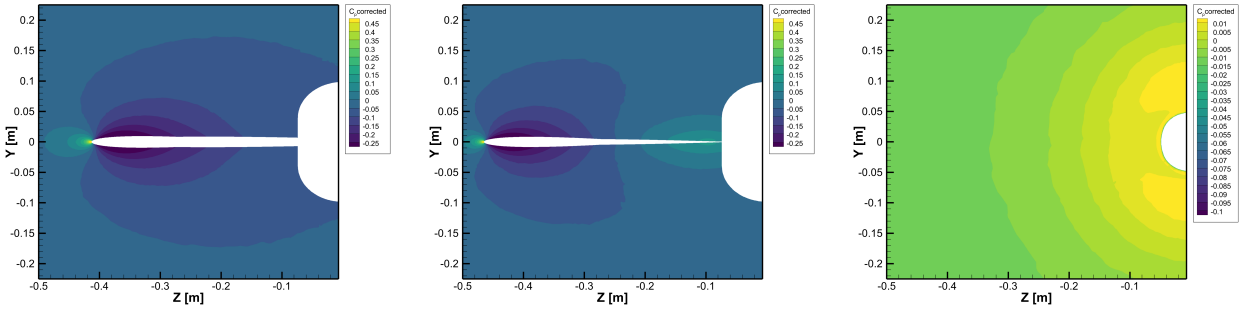
(c) $Re = 3.9$ **Million/meter**

(d) $Re = 2.8$ **Million/meter**

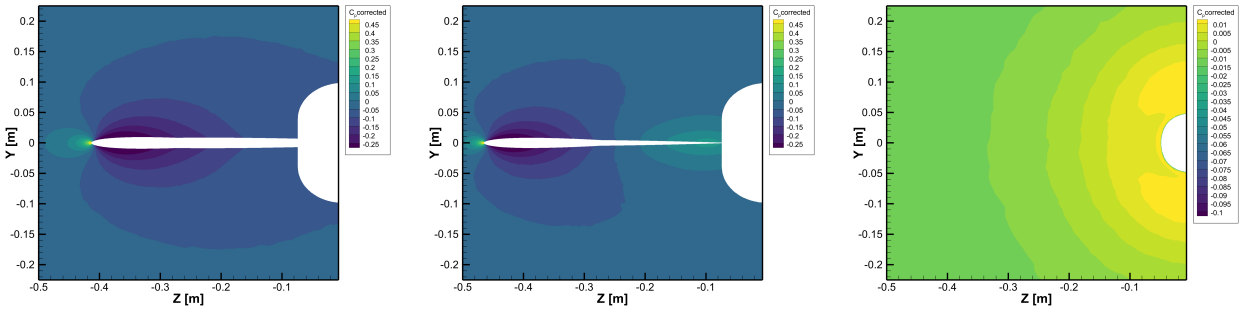
Fig. 24 Submission D as-designed model-in. Velocity magnitude contour downstream of the model at $x = 5.0888$ m, across three Reynolds numbers. The streamline overlay at $Re = 2.8$ Million/meter highlights the in-plane streamlines.



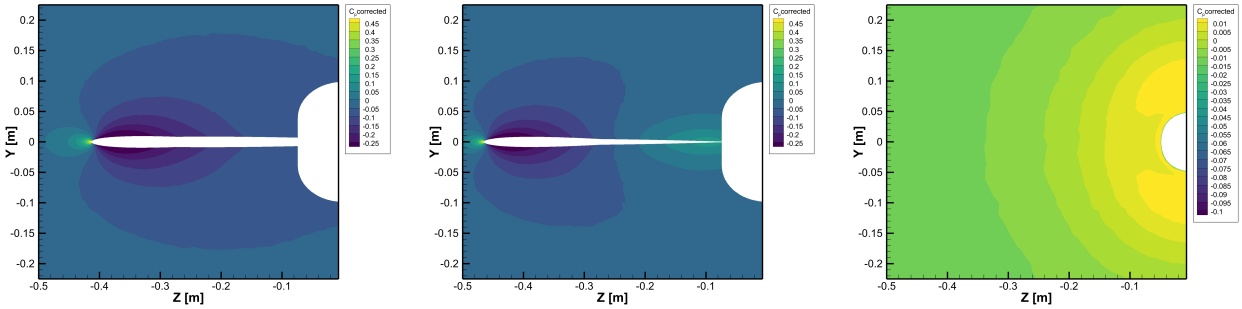
(a) Extraction locations



(b) $Re = 1.7$ **Million/meter,** $x = 4.146$ **m** **(c)** $Re = 1.7$ **Million/meter,** $x = 4.1855$ **m** **(d)** $Re = 1.7$ **Million/meter,** $x = 4.772$ **m**

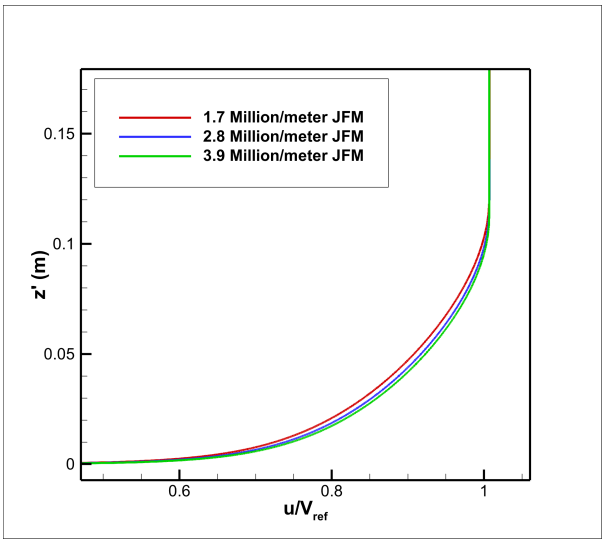


(e) $Re = 2.8$ **Million/meter,** $x = 4.146$ **m** **(f)** $Re = 2.8$ **Million/meter,** $x = 4.1855$ **m** **(g)** $Re = 2.8$ **Million/meter,** $x = 4.772$ **m**

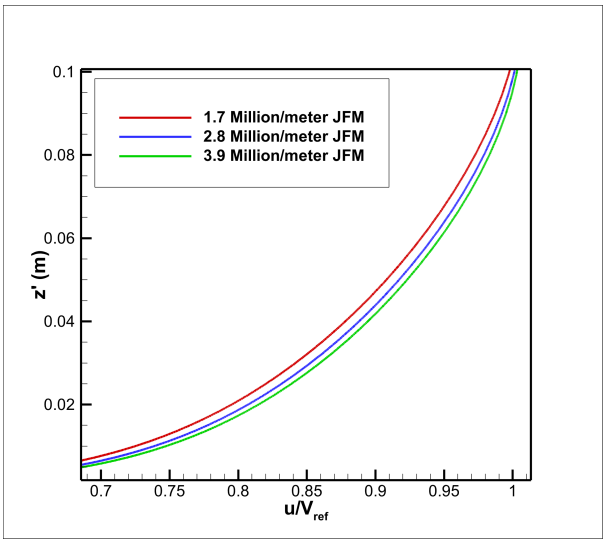


(h) $Re = 3.9$ **Million/meter,** $x = 4.146$ **m** **(i)** $Re = 3.9$ **Million/meter,** $x = 4.1855$ **m** **(j)** $Re = 3.9$ **Million/meter,** $x = 4.772$ **m**

Fig. 25 Submission D as-designed model-in: extraction locations (top-left) and C_p contours at the three CFD extraction stations across three Reynolds numbers. Rows correspond to Reynolds number (1.7, 2.8, 3.9 M/m); columns correspond to streamwise station ($x = 4.146$, 4.1855, 4.772 m).

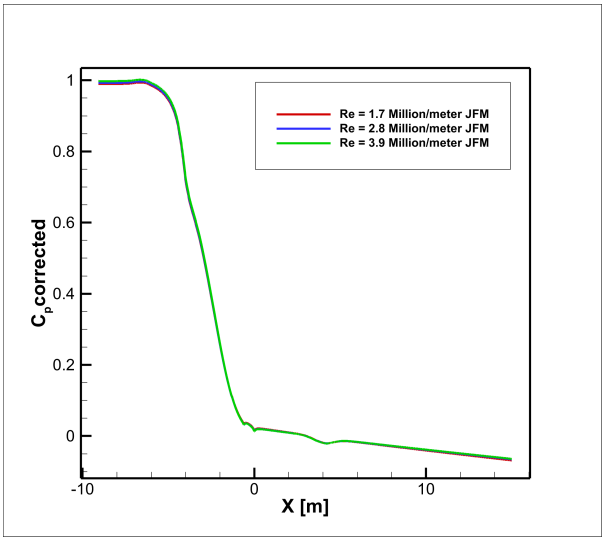


(a) Full profile

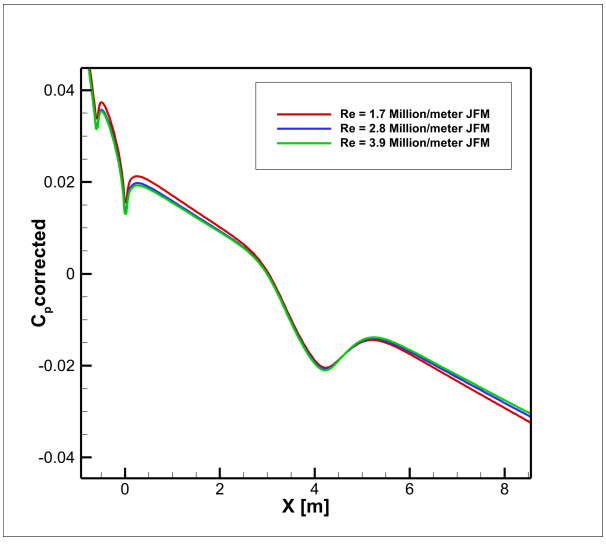


(b) Near-wall detail

Fig. 26 Reynolds number effects on the boundary layer profile at $x = 5.0888$ m.

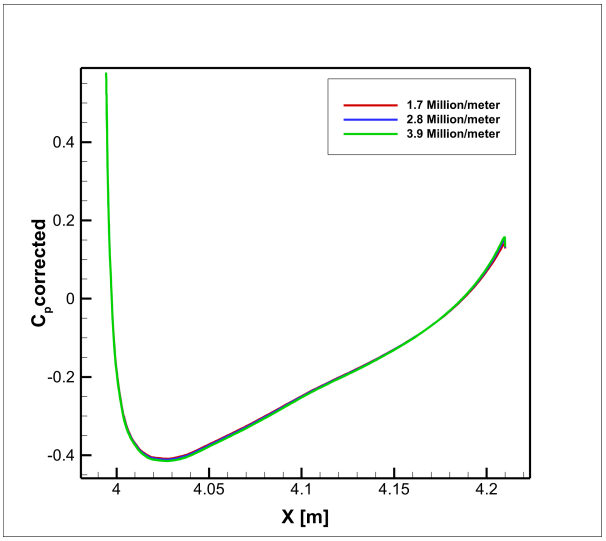


(a) Full distribution

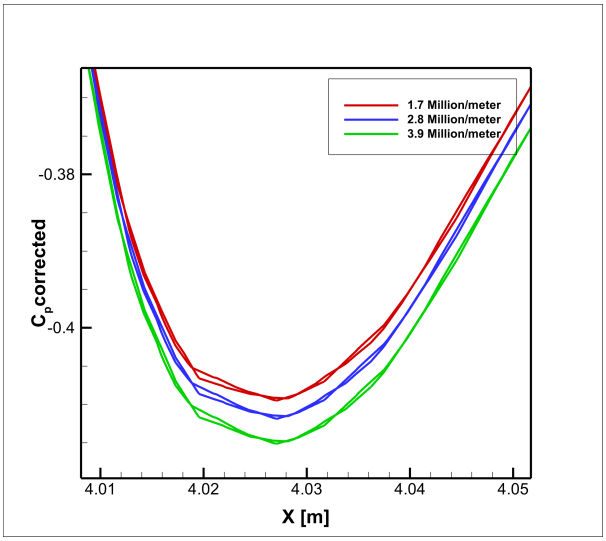


(b) Test section view

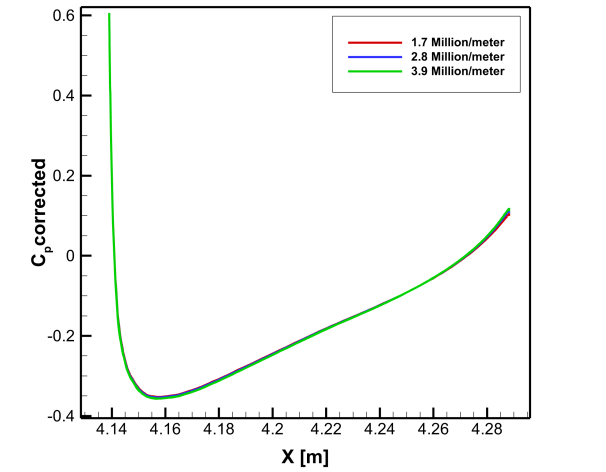
Fig. 27 Reynolds number effects on the pressure coefficient along the centerline of the starboard wall.



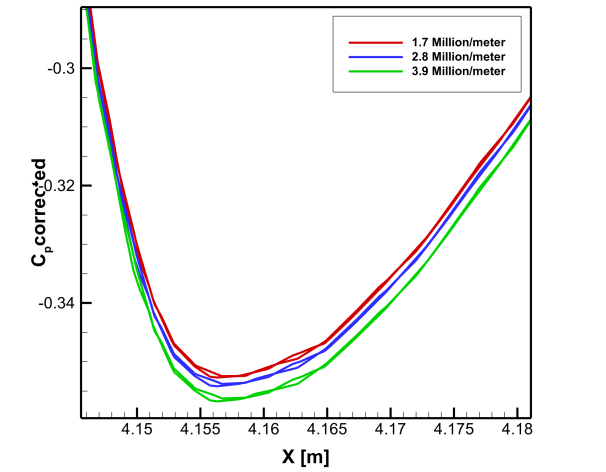
(a) $z = -0.214$ **m, full chord**



(b) $z = -0.214$ **m, leading-edge detail**



(c) $z = -0.404$ **m, full chord**



(d) $z = -0.404$ **m, leading-edge detail**

Fig. 28 Pressure coefficient on the wing at two spanwise stations.

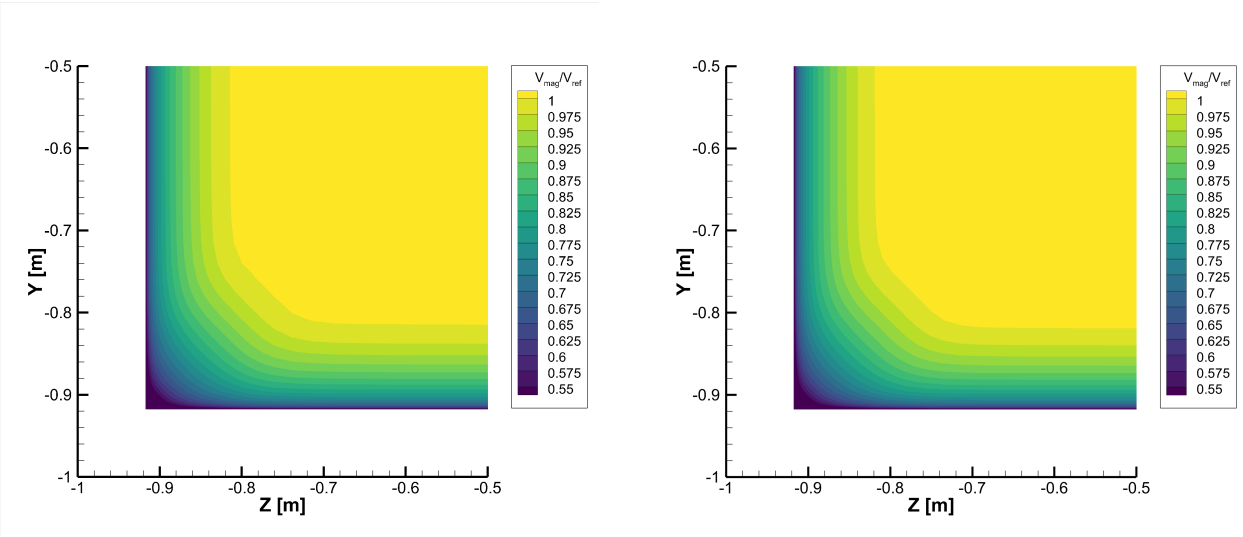
VII. Model-in vs. Empty Tunnel

A direct comparison between the model-in and empty-tunnel configurations at matched freestream conditions isolates the influence of the model on the tunnel flow field. Velocity magnitude contours, boundary layer profiles, and wall pressure distributions at the same streamwise stations are used for this comparison.

The presence of the model produces a marked acceleration of the flow alongside the test section and a corresponding reduction in wall boundary layer thickness, as evident in the velocity magnitude contours, Figure 29. This behavior is consistent with the blockage imposed by the model, which displaces flow toward the tunnel walls and imposes a favorable pressure gradient on the wall boundary layer. The streamline topology, however, remains broadly consistent between the two configurations, indicating that the global flow organization in the test section is preserved.

Boundary layer profiles extracted along the starboard wall centerline downstream of the model show a thinner and visibly disturbed boundary layer in the model-in case relative to the empty-tunnel baseline, Figure 30. The reduction in thickness reflects the upstream acceleration imposed by blockage, while the distortion of the profile shape reflects the imprint of the model pressure field on the wall flow.

The starboard wall pressure coefficient distributions in Figure 31 corroborate this picture. The model-in C_p exhibits a marked decrease relative to the empty-tunnel baseline in the region alongside the model, consistent with the local flow acceleration imposed by blockage.



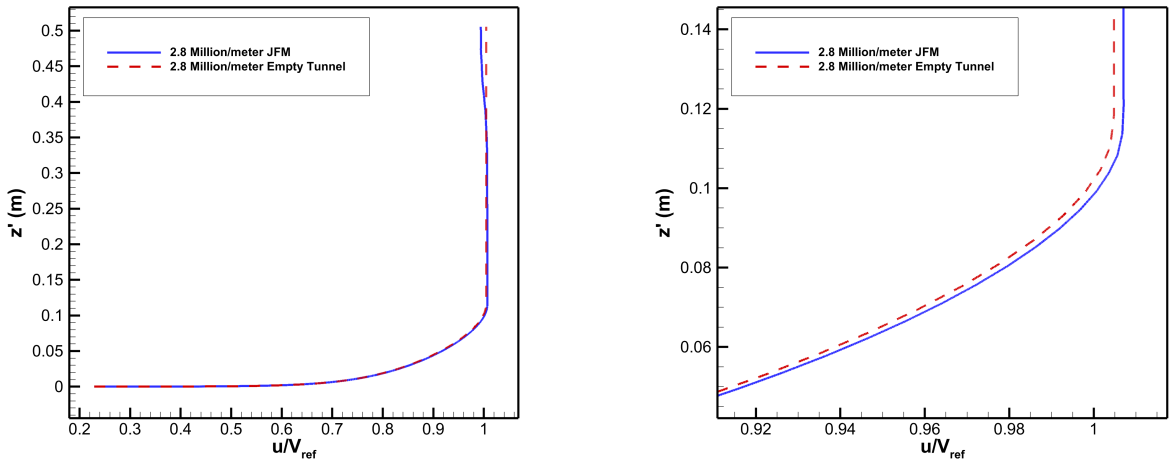
(a) $Re = 2.8$ **Million/meter Empty Tunnel**

(b) $Re = 2.8$ **Million/meter JFM**

(c) $Re = 2.8$ **Million/meter Empty Tunnel**

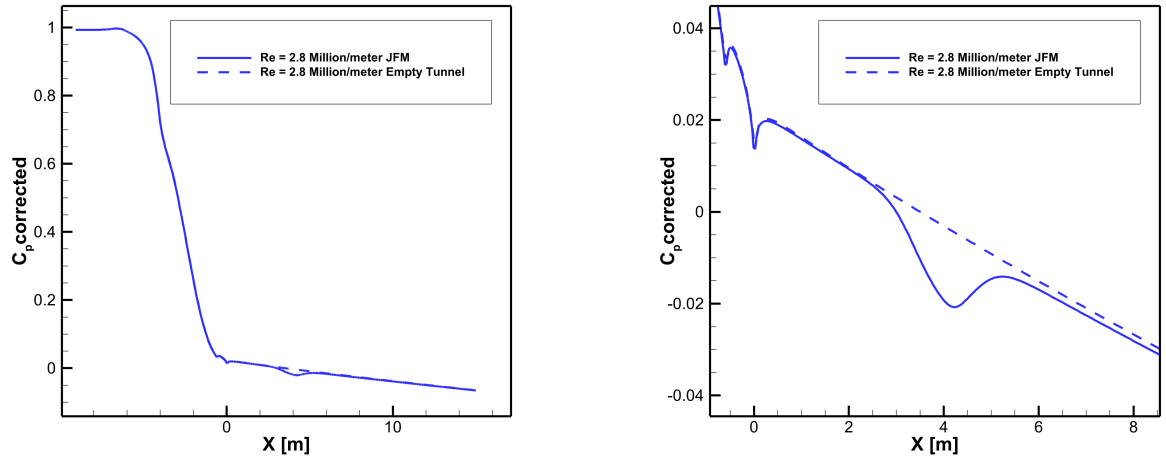
(d) $Re = 2.8$ **Million/meter JFM**

Fig. 29 Submission D as-designed model-in and empty-tunnel case. Velocity magnitude contour downstream of the model at $x = 5.0888$ m. The streamline overlay highlights the in-plane streamlines.



(a) Full profile for BL **(b) BL edge**

Fig. 30 Boundary layer profile at $x = 5.0888$ m for empty tunnel and model-in case at $Re = 2.8$ Million/meter case.



(a) Full distribution **(b) Test-section view**

Fig. 31 Pressure coefficient along the starboard wall, model-in vs. empty-tunnel comparison.

VIII. Preliminary Best Practices for the Model-in Case

1. Minimize interference from the model support system

The geometry of both the computational and experimental support hardware should be selected to minimize aerodynamic interference with the flow around the model. Sting and strut cross-sections should be sized to satisfy structural requirements without introducing pressure disturbances that propagate into the region of interest, and any fairings or transitions should be shaped to avoid local separation and minimize juncture flow effects. Where geometric simplification of the support is possible without compromising the validation objective, it should be adopted.

2. Smooth nonessential geometric features on the model

Features on the model that do not contribute to the intended flow physics, such as fastener heads, panel gaps, and pressure tap fittings, should be smoothed. Retaining such features incurs substantial meshing cost and can introduce localized flow disturbances that are difficult to resolve consistently across solvers, without contributing to the validation objective. Geometric simplification should be documented and justified against the quantities of interest.

3. Outflow boundary conditions from the empty-tunnel case may be applicable to the model-in case

The inflow and outflow boundary conditions established for the empty-tunnel configuration were found to be sufficient for the model-in case for the extended test section configuration presented in this paper. The streamwise distance between the inflow plane and the model is large enough that the freestream conditions are governed by the upstream contraction and settling chamber rather than by the presence of the model. These findings may change when the model supports and sting is included in the CFD mesh or if the wake is resolved behind the fuselage of the model.

IX. Acknowledgments

The authors would like to thank the Office of Naval Research, in particular Dr. Julie Young, for their support of this research under research grant number N00014-22-1-2660. Additional funding was provided by the Kevin T. Crofton Department of Aerospace and Ocean Engineering. The authors also thank William Oetjens of the Virginia Tech Stability Wind Tunnel for his support during the experimental measurements. The scale of this effort could not have been achieved without the help of several of our undergraduate and graduate research students. Specifically, we would like to thank Rujipa Shayutapong, Jaedyn Williams, ThanhLong Duong, Maiann Borgoltz, Kevin Xu, William Estes, Aditya Thota and Aidan Bell. Lastly, the authors are very grateful to the AOE Machine Shop, for their support and assistance with the fabrication and assembly of crucial hardware for the validation effort.

A. Appendix

A. Empty-Tunnel Calibration Procedure

This appendix details the four-step calibration procedure summarized in Section IV.B, by which model-in CFD pressure coefficients are referenced to the freestream condition established in an empty-tunnel simulation. The pressure coefficients used throughout this procedure are defined relative to the upstream contraction and settling chamber stations as

$$C_p = \frac{P - P_C}{P_S - P_C}, \tag{5}$$

where P is the local static pressure, P_C is the contraction reference pressure, and P_S is the settling chamber reference pressure. The settling chamber pressure P_S is assumed to be approximately equal to the freestream stagnation pressure, and the difference $P_S - P_C$ therefore serves as a proxy for the freestream dynamic pressure $\frac{1}{2}\rho_\infty U_\infty^2$. This formulation eliminates the need to evaluate ρ_∞ and U_∞ explicitly and ensures that the calibration is constructed entirely from upstream pressure measurements that are insensitive to the presence of a model.

Step 1: Empty test-section calibration. An empty test-section simulation is run at the target Reynolds number, and P_∞ is extracted at the tunnel center of rotation. The empty-tunnel calibration coefficients are evaluated at the contraction

and settling chamber stations,

$$C_{p,C}^{\mathrm{ET}} = \frac{P_C^{\mathrm{ET}} - P_\infty^{\mathrm{ET}}}{P_S^{\mathrm{ET}} - P_C^{\mathrm{ET}}}, \qquad C_{p,S}^{\mathrm{ET}} = \frac{P_S^{\mathrm{ET}} - P_\infty^{\mathrm{ET}}}{P_S^{\mathrm{ET}} - P_C^{\mathrm{ET}}}, \tag{6}$$

where the superscript ET denotes empty-tunnel quantities. The pair $\left(C_{p,C}^{\mathrm{ET}},\ C_{p,S}^{\mathrm{ET}}\right)$ constitutes the empty-tunnel calibration relationship and is recorded for use in the subsequent model-in correction step.

Step 2: Match the model-in freestream to the empty-tunnel freestream. A model-in simulation, e.g. the Juncture Flow Model (JFM) installed in the test section, is run, and the upstream contraction and settling chamber pressures P_C^{MI} and P_S^{MI} are recorded. The back-pressure boundary condition of the model-in simulation is iteratively adjusted until these upstream pressures are consistent with the empty-tunnel freestream condition, so that the two simulations share a common freestream reference.

Step 3: Compute uncorrected model-in pressure coefficients. With the freestream conditions matched, model-in surface and field pressure coefficients are computed using the contraction and settling chamber pressures rather than a local test-section pressure, since the latter is contaminated by the presence of the model. The uncorrected model-in coefficient at any location of interest is

$$C_p^{\mathrm{MI,\,uncorr}} = \frac{P^{\mathrm{MI}} - P_C^{\mathrm{MI}}}{P_S^{\mathrm{MI}} - P_C^{\mathrm{MI}}}. \tag{7}$$

Step 4: Apply the empty-tunnel calibration correction. The uncorrected coefficient from Eq. (7) is remapped through the empty-tunnel calibration coefficients of Eq. (6) so that the model-in result is referenced to the same freestream condition used in the empty-tunnel case,

$$C_p^{\mathrm{MI,\,corr}} = C_p^{\mathrm{MI,\,uncorr}} \left(C_{p,S}^{\mathrm{ET}} - C_{p,C}^{\mathrm{ET}}\right) + C_{p,C}^{\mathrm{ET}}. \tag{8}$$

This linear remapping is equivalent to referencing the model-in pressure coefficients to an effective freestream pressure

$$P_\infty^{\mathrm{eff}} = \frac{C_{p,S}^{\mathrm{ET}}\, P_C^{\mathrm{MI}} - C_{p,C}^{\mathrm{ET}}\, P_S^{\mathrm{MI}}}{C_{p,S}^{\mathrm{ET}} - C_{p,C}^{\mathrm{ET}}}, \tag{9}$$

constructed from the empty-tunnel calibration coefficients and the model-in upstream pressures. Following Eq. (8), the corrected model-in pressure coefficients are directly comparable to experimental data referenced through the same calibration. The step-by-step effect of the calibration process on the wall centerline C_p can be observed in Figure 32.

add small blue square and black sqaure on image like in legend

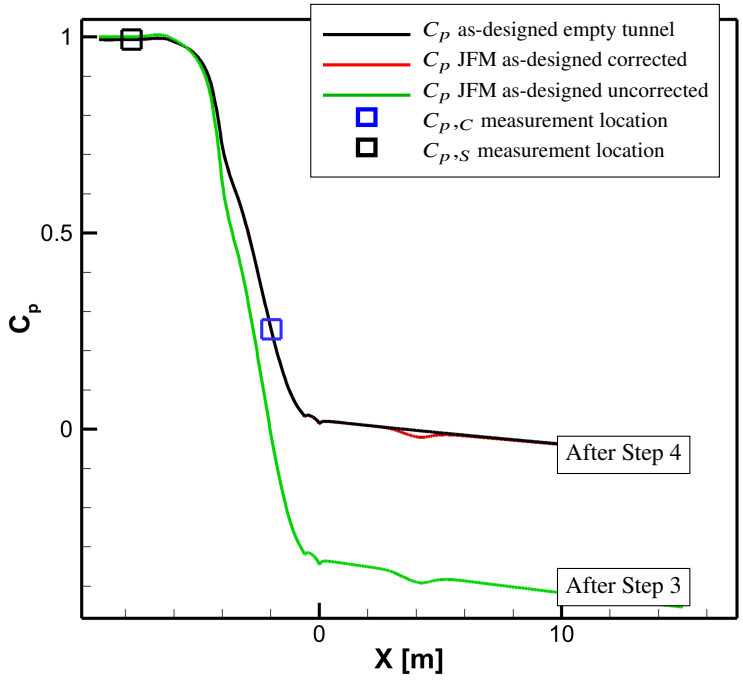
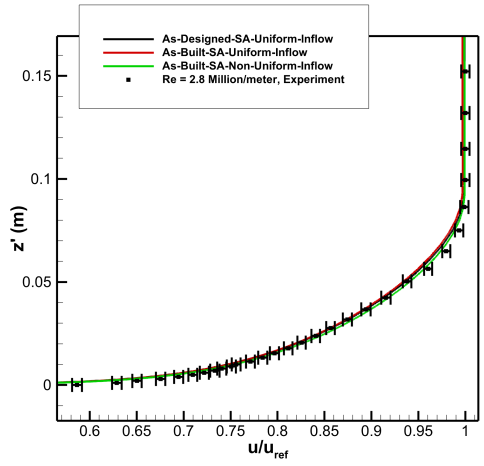
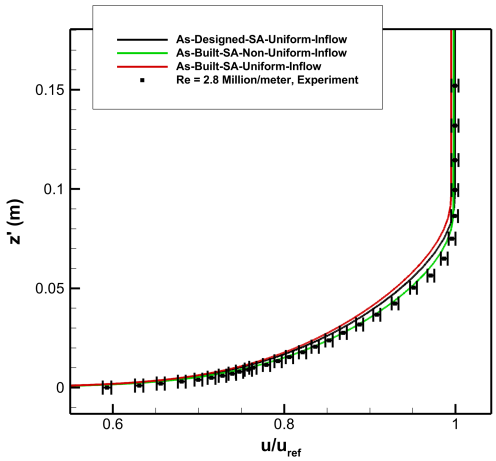


Fig. 32 Effect of the empty-tunnel calibration on the model-in C_p distribution. The corrected curve references the model-in pressure to the freestream condition established by the empty-tunnel calibration, enabling direct comparison with experimental data.

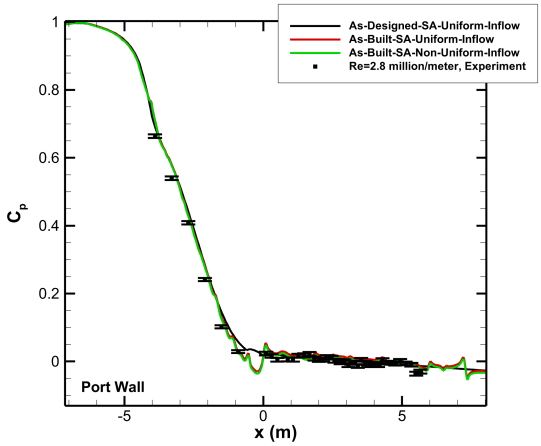
B. Empty-Tunnel Contours and Line Plots



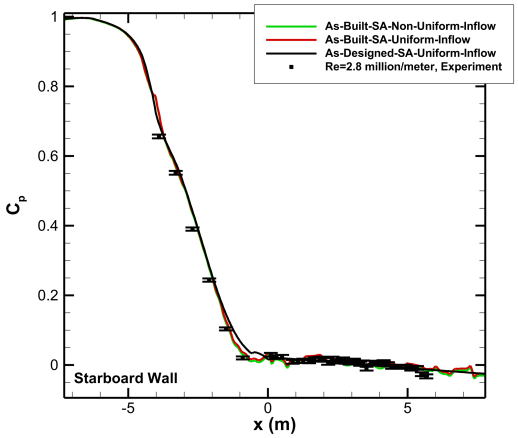
(a) BL profile #1 on port wall



(b) BL profile #1 on starboard wall



(c) C_p at port wall centerline



(d) C_p at starboard wall centerline

Fig. 33 Boundary layer profiles and pressure coefficient distributions. z' represents the wall-normal distance for the BL extractions.

References

[1] Oberkampf, W. L., and Trucano, T. G., "Verification and Validation in Computational Fluid Dynamics," *Progress in Aerospace Sciences*, Vol. 38, No. 3, 2002, pp. 209–272. https://doi.org/10.1016/S0376-0421(02)00005-2.

[2] Roache, P. J., *Verification and Validation in Computational Science and Engineering*, Hermosa Publishers, Albuquerque, NM, 1998.

[3] Babuška, I., Oberkampf, W. L., and Roy, C. J., "NISTIR 8298: Verification, Validation, and Uncertainty Quantification in Scientific Computing," Tech. Rep. NISTIR 8298, National Institute of Standards and Technology, 2021. https://doi.org/10.6028/NIST.IR.8298.

[4] Oberkampf, W. L., Roy, C. J., and Ferson, S., "Assessment and Validation of Engineering Models," *Computers & Mathematics with Applications*, Vol. 55, No. 7, 2008, pp. 1493–1513. https://doi.org/10.1016/j.camwa.2007.06.011.

[5] Melber-Wilkending, S., Kuhlmann, T., and Warschkow, A., "CFD Simulation of Complete Wind Tunnels as a Contribution to Tunnel-to-Tunnel Correlation," *45th AIAA Aerospace Sciences Meeting and Exhibit*, Reno, NV, 2007. https://doi.org/10.2514/6.2007-1055, aIAA-2007-1055.

[6] Rogers, S. E., Slotnick, J. P., and Kleb, W. L., "CFD Simulations of Wind Tunnel Effects on High-Lift Configurations," *18th AIAA Applied Aerodynamics Conference*, Denver, CO, 2000. https://doi.org/10.2514/6.2000-4223, aIAA-2000-4223.

[7] Detomaso, T., Iaccarino, G., Pečnik, R., and Hickel, S., "Quantification of Uncertainties in CFD Simulations Using a Transonic Wind Tunnel Test Case," *AIAA Journal*, Vol. 58, No. 4, 2020, pp. 1467–1481. https://doi.org/10.2514/1.J058595.

[8] Rumsey, C. L., Morrison, J. H., and Biedron, R. T., "NASA Juncture Flow Experiment: Description and Boundary Conditions," Tech. Rep. NASA/TM-2017-219611, NASA Langley Research Center, 2017.

[9] Rumsey, C. L., Morrison, J. H., Biedron, R. T., and Lee-Rausch, E. M., "Overview of the NASA Juncture Flow Experiment: Goals, Setup, and CFD Comparisons," *AIAA Journal*, Vol. 56, No. 7, 2018, pp. 2730–2747. https://doi.org/10.2514/1.J056696.

[10] Rumsey, C. L., Morrison, J. H., Biedron, R. T., et al., "Lessons Learned from the NASA Juncture Flow CFD Validation Experiment," Tech. Rep. NASA/TM-20210015434, NASA Langley Research Center, 2021.

[11] Borgoltz, A., Intaratep, N., Devenport, W. J., Roy, C. J., and Hoge-Patil, A. S., "VT Stability Tunnel: Experimental Characterization of Boundary Conditions for Subsonic Wind Tunnels," *AIAA AVIATION Forum*, San Diego, CA, 2026. To appear.

[12] Roy, C. J., Hogepatil, A. S., Borgoltz, A., Devenport, W. J., Lowe, K. T., and Shane, D., "Computational Fluid Dynamics Comparisons for the Virginia Tech Stability Wind Tunnel," *AVT-391 Specialists' Meeting on Experimental and Computational Assessment of Flow Instabilities and Noise Generation*, NATO Science and Technology Organization, Neuilly-sur-Seine, France, 2025. https://doi.org/10.14339/MP-AVT-391-08.

[13] Rumsey, C. L., Ahmad, N. N., Carlson, J.-R., Kegerise, M. A., Neuhart, D. H., Hannon, J. A., Jenkins, L. N., Yao, C.-S., Balakumar, P., Gildersleeve, S., Bartram, S. M., Pulliam, T. H., Olsen, M. E., and Spalart, P. R., "NASA Juncture Flow Computational Fluid Dynamics Validation Experiment," *AIAA Journal*, Vol. 60, No. 8, 2022, pp. 4789–4807. https://doi.org/10.2514/1.J061600.

[14] Eça, L., Hoekstra, M., Beja Pedro, J. F., and Falcão de Campos, J. A. C., "On the Characterization of Grid Density in Grid Refinement Studies for Discretization Error Estimation," *International Journal for Numerical Methods in Fluids*, Vol. 72, No. 2, 2013, pp. 119–134. https://doi.org/10.1002/fld.3733.

[15] Cadence Design Systems, Inc., "Pointwise Mesh Generation Software," , 2025. Version 18.6R1, Fort Worth, TX.

[16] Rumsey, C. L., "Turbulence Modeling Resource," https://turbmodels.larc.nasa.gov/, 2026. Accessed 2026.

[17] AIAA Applied Aerodynamics Technical Committee, "AIAA CFD Drag Prediction Workshop," https://aiaa-dpw.larc.nasa.gov/, 2026. Accessed 2026.

[18] AIAA Applied Aerodynamics Technical Committee, "AIAA CFD High Lift Prediction Workshop," https://hiliftpw.larc.nasa.gov/, 2026. Accessed 2026.

[19] Duetsch-Patel, J. E., Gargiulo, A., Lowe, K. T., Devenport, W. J., and Roy, C. J., "The BeVERLI Hill Experiments for Smooth-Body Turbulent Flow Separation," *34th Congress of the International Council of the Aeronautical Sciences*, 2024.

[20] Duetsch-Patel, J. E., et al., "Strategies for Computational Fluid Dynamics Validation Experiments," *Journal of Verification, Validation and Uncertainty Quantification*, Vol. 8, No. 3, 2023, p. 031004. https://doi.org/10.1115/1.4062669.

[21] Roy, C. J., and Blottner, F. G., "Methodology for Turbulence Model Validation: Application to Hypersonic Flows," *Journal of Spacecraft and Rockets*, Vol. 40, No. 3, 2003, pp. 313–325. https://doi.org/10.2514/2.3966.

[22] Glegg, S. A. L., and Devenport, W. J., *Aeroacoustics of Low Mach Number Flows: Fundamentals, Analysis, and Measurement*, 2nd ed., Academic Press, London, 2024.

[23] Ahmad, N. N., Rumsey, C. L., and Carlson, J.-R., "In-Tunnel Simulations of the NASA Juncture Flow Model," *AIAA Scitech 2021 Forum*, 2021. https://doi.org/10.2514/6.2021-1428, aIAA-2021-1428.



https://dspace.org/

VT stability tunnel: recommendations for CFD model validation in subsonic wind tunnels

Hoge Patil, Adwait; Roy, Christopher J.; Devenport, William J.; Borgoltz, Aurelien; Intaratep, Nanyaporn ...

2026-06-08
American Institute of Aeronautics and Astronautics (AIAA)
https://doi.org/10.2514/6.2026-4460
HogePatil A, Roy CJ, Devenport WJ, et al., (2026) VT stability tunnel: recommendations for CFD model validation in subsonic wind tunnels. In: AIAA AVIATION 2026 Forum, 8-12 Jun 2026, San Diego, Article number 2026-4460

Downloaded from a DSpace repository. https://dspace.org/